

## RESEARCH ARTICLE

10.1002/2013JA019517

## Key Points:

- $O^+$  and  $H^+$  density maps at the magnetospheric equatorial plane are produced
- $O^+$  and  $H^+$  density variation with geomagnetic and solar activity are analyzed
- The direct entry of  $O^+$  ions at low geocentric distances is confirmed

## Correspondence to:

R. Maggiolo,  
maggiolo@aeronomie.be

## Citation:

Maggiolo, R., and L. M. Kistler (2014), Spatial variation in the plasma sheet composition: Dependence on geomagnetic and solar activity, *J. Geophys. Res. Space Physics*, 119, 2836–2857, doi:10.1002/2013JA019517.

Received 7 OCT 2013

Accepted 1 APR 2014

Accepted article online 3 APR 2014

Published online 24 APR 2014

## Spatial variation in the plasma sheet composition: Dependence on geomagnetic and solar activity

R. Maggiolo<sup>1</sup> and L. M. Kistler<sup>2</sup>

<sup>1</sup>Belgian Institute for Space Aeronomy, Brussels, Belgium, <sup>2</sup>Space Science Center, University of New Hampshire, Durham, New Hampshire, USA

**Abstract** We study the spatial distribution of plasma sheet  $O^+$  and  $H^+$  ions using data from the COmposition and DIstribution Function (CODIF) instrument on board the Cluster spacecraft from 2001 to 2005. The densities are mapped along magnetic field lines to produce bidimensional density maps at the magnetospheric equatorial plane for various geomagnetic and solar activity levels (represented by the  $Kp$  and  $F_{10.7}$  indexes). We analyze the correlation of the  $O^+$  and  $H^+$  density with  $Kp$  and  $F_{10.7}$  in the midtail region at geocentric distances between 15 and 20  $R_E$  and in the near-Earth regions at radial distances between 7 and 8  $R_E$ . Near Earth the  $H^+$  density slightly increases with  $Kp$  and  $F_{10.7}$  while in the midtail region it is not correlated with  $Kp$  and  $F_{10.7}$ . On the contrary, the amount of  $O^+$  ions significantly increases with  $Kp$  and  $F_{10.7}$  independently of the region. In the near-Earth region, the effects of solar EUV and geomagnetic activity on the  $O^+$  density are comparable. In the midtail region, the  $O^+$  density increases at a lower rate with solar EUV flux but strongly increases with geomagnetic activity although the effect is modulated by the solar EUV flux level. We also evidence a strong increase of the proportion of  $O^+$  ions with decreasing geocentric distance below  $\sim 10 R_E$ . These results confirm the direct entry of  $O^+$  ions into the near-Earth plasma sheet and suggest that both energetic outflows from the auroral zone and cold outflow from the high-latitude ionosphere may contribute to feed the near-Earth plasma sheet with ionospheric ions.

### 1. Introduction

The magnetospheric plasma composition depends on the relative contribution of the solar wind, consisting mainly of  $H^+$  ( $\sim 95\%$ ) and  $He^{++}$  ( $\sim 5\%$ ) and of the ionosphere, consisting mainly of  $H^+$ ,  $O^+$ , and  $He^+$ . The plasma composition is a key issue, as heavy ionospheric  $O^+$  ions play an important role in magnetospheric dynamics [see Lotko, 2007, and references therein]. They have larger gyroradii than  $H^+$  and consequently affect the plasma typical scale sizes. They also contribute significantly to the plasma mass density, a parameter which plays a significant role for the energy transport, through the Alfvén velocity, for instability development like the Kelvin-Helmoltz instability, for dispersion relations, and for energy conversion through magnetic reconnection. Furthermore,  $O^+$  ions are almost exclusively of ionospheric origin and represent good tracers of ionospheric sources.

Ionospheric plasma is cold and must be energized in order to overcome the Earth's gravity and escape into the magnetosphere. At low altitudes, ionospheric particles are ionized and heated by solar photoemissions and particle precipitation. Ionization and heating processes control the ion scale height and condition the particle flux that access higher altitudes where further energization can occur.

The energy is provided by the Sun through two pathways. Ionospheric ions are essentially created through photoionization of atmospheric neutral atoms mainly by solar ultraviolet (UV), extreme ultra violet (EUV), and to a less extent by soft X-ray. In the following, solar photoemissions that contribute to ionize and heat ionospheric material will be referred to as solar EUV emissions. Solar photoemissions energize ionospheric material to low energies (EUV photons energy ranges between  $\sim 10$  eV and  $\sim 120$  eV). Consequently, the main effect of solar irradiance is to control the flux of ionospheric particles that reach a sufficiently high altitude to be further heated and energized. However, it can also have an effect on ionospheric ion transport and energization, such as in the auroral zone where it modulates acceleration processes [Newell *et al.*, 1996, 1998; Peterson *et al.*, 2006] or above the polar caps where it is correlated with the  $O^+$  and  $H^+$  outflow velocities [Abe *et al.*, 2004]. On the other hand, energy is transferred through the coupling between the solar wind and the magnetosphere. The solar wind energy can be transferred to the ionosphere either directly, in particular

in the cusp region (dayside reconnection), or via the magnetospheric system (tail reconnection). This coupling plays a significant role for ionospheric outflow. At low altitudes, it modulates the precipitation of solar wind and magnetospheric particles which contribute to the ionization and heating of ionospheric particles [Newell *et al.*, 2009]. It also increases frictional heating that can drive field-aligned flow in the *F* region of the ionosphere [e.g., Heelis *et al.*, 1992; Wahlund *et al.*, 1992]. At higher altitude it modulates particle acceleration [e.g., Norqvist *et al.*, 1998] and transport as it drives magnetospheric field line convection.

The energy input from the Sun to the magnetosphere and ionosphere—and consequently ionospheric outflows—are modulated by the solar cycle. The solar EUV flux increases with solar activity following the 11 year solar cycle. Geomagnetic active periods associated with the release of energy stored in the magnetosphere occur on timescales of some hours to some days, and their occurrence frequency increases with increasing solar activity [Hansen *et al.*, 1976; Feynman, 1982]. Consequently, ionospheric outflows are intense during solar maximum and weaken as the solar activity decreases [e.g., Yau *et al.*, 1985a].

The main outflow regions are located at high magnetic latitudes. Above the polar cap, polar wind particles are accelerated by the ambipolar electric field caused by the charge separation between the light electrons and heavy ions [Axford, 1968]. In this classical description, the acceleration is too low to allow  $O^+$  ions to reach their escape velocity. However, observations show the presence of upflowing  $O^+$  ions above the polar caps, which may be due to further acceleration mechanisms (nonclassical polar wind) [see Yau *et al.*, 2007, and references therein]. At lower latitudes, the auroral region is a major source of ionospheric plasma. Auroral outflow occurs on closed field lines and are particularly intense in the nightside auroral region where magnetospheric lines are connected to the tail regions where energy is released during active periods. In this region, the ionization results largely from particle precipitation. Intense outflows also occur in the dayside ionosphere at the ionospheric projection of the cusp where solar wind particle and energy directly precipitate in the ionosphere [Lockwood *et al.*, 1985]. In this region the extraction of  $O^+$  ions and their energization is controlled by the inflow of magnetosheath plasma into the cusp [Lennartsson *et al.*, 2004] and by the solar illumination level [Peterson *et al.*, 2006].

The transport of ionospheric particles from low altitudes to the plasma sheet is a combination of their motion along the magnetic field lines and of the magnetic field lines convection. While ionospheric ions are transported in the magnetosphere, they can undergo further energization, in particular through centrifugal acceleration [Cladis, 1986]. Centrifugal acceleration is small but can be important for the slower particles as they are subject to it for a long time [Nilsson *et al.*, 2010]. During active periods, tailward convection is increased, and ionospheric particles reach the plasma sheet at lower geocentric distances. There is a significant amount of  $O^+$  and  $H^+$  ions in transit from the ionosphere to the magnetosphere [Peterson *et al.*, 2008; Liao *et al.*, 2010; Yau *et al.*, 2012]. Consequently, the increase of convection during active periods considerably enhances ionospheric particle flow into the plasma sheet [Cully *et al.*, 2003b; Ebihara *et al.*, 2006; Haaland *et al.*, 2009, 2012]. In addition, Liao *et al.* [2012] showed that there is also a strong solar cycle dependence in the amount of  $O^+$  flowing from the lobe region to the plasma sheet.

Ionospheric particle trajectory simulations reveal that ionospheric ions can reach the plasma sheet at geocentric distances well outside of  $20 R_E$  [Delcourt *et al.*, 1990; Moore and Delcourt, 1995; Ebihara *et al.*, 2006]. Once ionospheric particles enter the plasma sheet they are isotropized and energized. Modeling studies have shown that since their first crossing of the neutral sheet, they are accelerated to energies above 1 keV [Chappell *et al.*, 2000; Ebihara *et al.*, 2006; Kitamura *et al.*, 2010]. In the plasma sheet, ionospheric ions are transported in the earthward direction and are further energized.

The modulation of ionospheric outflow and ionospheric ion transport result in changes in the magnetospheric plasma composition. Our knowledge of the magnetospheric plasma composition is based on in situ measurements. Since the first detection of  $O^+$  in the magnetosphere by Shelley *et al.* [1972], a wide range of observations has shown that  $O^+$  represents an important fraction of the magnetospheric plasma. At times, the ionospheric source is thought to be the dominant source of magnetospheric plasma [Chappell *et al.*, 1987]. Several studies have analyzed the magnetospheric  $O^+$  content and its dependence on geomagnetic activity and solar EUV flux in various magnetospheric regions.  $O^+$  ions have been detected everywhere from the near-Earth magnetosphere [Young *et al.*, 1982; Kronberg *et al.*, 2012] to the middle and far magnetospheric tail [Lennartsson, 1989; Nosé *et al.*, 2009; Moukik *et al.*, 2010]. Independent of the region and of the energy range, the  $O^+$  density is enhanced when solar EUV flux and geomagnetic activity increase.

These studies are based on measurements taken near the magnetospheric equatorial plane and are thus limited to specific regions, basically where the spacecraft orbit crosses the equatorial plane. The energy range and characteristics of ion detectors vary from one study to another, which restricts possible comparison between the densities in different magnetospheric regions. Recently, *Ohtani et al.* [2011] provided the first study of the  $O^+$  spatial distribution at large scales in the magnetosphere. Using Geotail density measurements near the magnetospheric equatorial plane, they produced  $5 \times 5 R_E$  maps of the  $O^+$  and  $H^+$  density in the tail plasma sheet. However, despite attempts to interpolate to lower energies, they used observations at energies (between 9 and 210 keV) above the average plasma sheet ions energy.

It is, however, possible to go beyond measurements taken near the equatorial plane to assess the density in the central plasma sheet. Indeed, the plasma density can be mapped along magnetic field lines if the plasma is isotropic. This mapping method has been discussed in detail and applied to the low-altitude DMSP spacecraft data to “image” the total ion density—the DMSP ion detector is not mass discriminating—in the plasma sheet [*Wing and Newell, 1998, 2002; Newell and Wing, 2000*].

In this study we apply a similar method to the  $O^+$  and  $H^+$  densities measured by the Cluster spacecraft to obtain for the first time detailed maps of the plasma sheet  $O^+$  and  $H^+$  density in the magnetospheric equatorial plane as a function of geomagnetic activity and solar EUV flux. In section 2 we describe the data and techniques used to map the data in the magnetospheric equatorial plane and compare our results with in situ measurements to assess the validity of the method. The density maps are then discussed in section 3. In section 4 we analyze the correlation of the  $O^+$  and  $H^+$  density with geomagnetic activity and solar EUV flux. Section 5 discusses in more details the spatial distribution of  $O^+$  and  $H^+$  ions in the plasma sheet. The results are discussed and summarized in section 6.

## 2. Data and Technique

### 2.1. Instrumentation and Data Selection

The four Cluster spacecraft were launched in 2000 into a nearly  $90^\circ$  inclination orbit with perigee around  $4 R_E$  and apogee around  $19 R_E$  geocentric distance. We use density measurements from the Cluster Ion Spectrometry (CIS)/CODIF experiment [*Rème et al., 2001*]. This high-resolution spectrometer measures the three-dimensional distribution function of the principal ion species in the energy range (40 eV–40 keV) and provides a full distribution function every 4–16 s depending on the operating mode. We use CODIF densities to produce statistical maps of the  $O^+$  and  $H^+$  density at the magnetospheric equatorial plane as a function of the solar EUV flux and of the geomagnetic activity. We perform this study using density measurements from 2001 to 2005 during the declining phase of the solar cycle. This time period has the advantage to cover a wide range of geomagnetic activity and solar activity levels while being short enough to minimize the potential effects of the instrument efficiency decrease with time. We use data from only one Cluster spacecraft (SC4). As we focus on the large-scale aspects of the plasma sheet density, adding data from the other Cluster satellites would not provide additional information.

We consider that partial densities between 1 keV and 40 keV as the count rate for  $O^+$  ions below 1 keV can be below the 1-count level. While outflowing ionospheric ions can have energies much lower than 1 keV, they are efficiently energized when they enter the plasma sheet where the typical  $H^+$  and  $O^+$  energy is higher than  $\sim 2$  keV [e.g., *Lennartsson and Shelley, 1986; Lennartsson, 1989; Bouhram et al., 2005*]. Therefore, the reduced energy range we use should not impact the  $O^+$  and  $H^+$  density presented in this study. This is confirmed by *Mouikis et al.* [2010] who showed for the same data set between 2001 and 2003 that considering densities between 1 and 40 keV does not have an effect on the density dependence on solar EUV flux and geomagnetic activity. We may, however, miss some  $H^+$  particles during cold dense plasma sheet intervals—occurring during prolonged quiet periods and thus quite rare—when the plasma sheet  $H^+$  ions temperature can be below 1 keV [e.g., *Terasawa et al., 1997; Fujimoto et al., 1998*]. Other cold populations that may be present in the region analyzed in this study, like plasmaspheric plumes [*Darrouzet et al., 2008*], are not considered.

To avoid contamination by high-energy particles from the radiation belts which can lead to wrong density estimate, we restrict our study to geocentric distances higher than  $6 R_E$ .

The variations of the solar UV/EUV flux are monitored by the daily averaged  $F_{10.7}$  index (a measure of the solar radio flux per unit frequency at a wavelength of 10.7 cm) which is a good proxy for the UV/EUV irradiance despite possible breakdown of the linear UV/EUV flux for high  $F_{10.7}$  values [Balan *et al.*, 1994]. To sort data as a function of the global geomagnetic activity level, we use the 3 h  $Kp$  index.

## 2.2. Mapping Technique

In order to produce two-dimensional density maps, we project the observed density along magnetic field lines to the magnetospheric equatorial plane. This method is based on theoretical and observational evidence indicating that the plasma sheet density can be mapped along magnetic field lines. Indeed, isotropic plasma density, temperature, and pressure remain constant along magnetic field lines [Spence *et al.*, 1989; Goertz and Baumjohann, 1991]. In the plasma sheet the isotropy is maintained by pitch angle scattering in the neutral sheet as long as the magnetic field line radius of curvature is small enough compared to the ion gyroradius [Lyons and Speiser, 1982; Sergeev *et al.*, 1993; Sergeev and Gvozdevsky, 1995]. At sufficiently high geocentric distances where the magnetic field line radius of curvature is high enough, the plasma sheet ions are mainly isotropic. This has been confirmed by several in situ observations [e.g., Lu *et al.*, 1992; Kistler *et al.*, 1992].

The densities are mapped along magnetospheric field lines using the Tsyganenko 96 (T96) magnetic field model [Tsyganenko, 1995; Tsyganenko and Stern, 1996] to compute the GSM coordinate of the field line at the magnetospheric equatorial plane, defined as the magnetic field reversal zone as obtained from the T96 model. The T96 model is an empirical model based on measurements and thus dominated by quiet time. We chose this model rather than more recent models like Tsyganenko 2001 and 2004 that are specifically designed for storm events and/or inner magnetosphere, as we exclude from our study the inner magnetosphere below  $6 R_E$  and very active periods.

Applying this technique requires a careful selection of data in order to isolate measurements taken in the isotropic plasma sheet. Only measurements satisfying certain conditions have been included. The main condition is that the plasma must be isotropic. This has been determined directly for  $H^+$  ions by imposing that the difference between the perpendicular and parallel  $H^+$  pressure computed over the whole CODIF energy range is lower than 20%. We do not apply the same criteria to the  $O^+$  ions. Indeed, while the  $H^+$  density in the plasma sheet is always sufficiently high to estimate accurately the parallel and perpendicular pressure, the  $O^+$  ion density is expected to be sometimes too low to do that (e.g., at large geocentric distances during periods of very low geomagnetic activity). By applying a similar criterion to  $O^+$  ions, we might introduce a bias in our statistics by removing regions of very low  $O^+$  density. We thus assume that if  $H^+$  ions are isotropic, then  $O^+$  ions are also isotropic (which should be correct as  $O^+$  ions have larger gyroradii than  $H^+$ ). However, outflowing ions of ionospheric origin can be present on the plasma sheet field lines, particularly those that map to the nightside auroral zone or that have recently reconnected and are populated with ions outflowing from the cusp region [e.g., Kistler *et al.*, 2010]. Outflowing ions are rich in  $O^+$  and are highly anisotropic with significant field-aligned velocity at Cluster altitude. Such outflows may thus not be removed by our criteria on  $H^+$  isotropy and may skew the  $O^+$  density estimate. To exclude them, we impose that the  $O^+$  field-aligned velocity is lower than 70 km/s which corresponds to an energy of  $\sim 410$  eV, well below the energy range considered in this study.

Before producing the maps, we add additional conditions to exclude regions which can straightforwardly be differentiated from the plasma sheet. We exclude the lobe region by imposing that the plasma pressure is higher than  $5 \cdot 10^{-2}$  nPa and the boundary layers and magnetosheath on the flanks by imposing that the ion perpendicular velocity is lower than 200 km/s and that the  $H^+$  density is lower than  $2 \text{ cm}^{-3}$  (it may exclude some cold dense plasma sheet intervals). This should also remove dynamical events in the plasma sheet like bursty bulk flows. We exclude the dayside magnetosheath/boundary layers and cusp region by excluding regions located in the dayside ( $X_{GSE} > 0$ ) and where the magnetic field magnitude is lower than 50 nT.

We only consider periods when  $Kp \geq 7$  and  $Dst \geq -200$  nT in order to exclude extremely disturbed periods when the plasma sheet  $O^+$  density can exceed the  $O^+$  density observed during large storms by 1 order of magnitude [see Mouikis *et al.*, 2010]. This can skew our statistic and result in a misleading representation of the plasma sheet composition dependence on geomagnetic activity.

We compute 1 min median density value from CODIF density measurements at full resolution satisfying all these criteria. After data selection has been made, 224,903 1 min samples are included in our statistics. Once mapped to the magnetospheric equatorial plane, the separation between two successive data points is lower than  $0.2 R_E$  for 86.2% of the data and lower than  $1 R_E$  for 98.5% of the data. We were thus able to produce two-dimensional maps with a resolution of  $1 R_E$  using modified coordinates  $X_{EQ}$  and  $Y_{EQ}$  where  $X_{EQ}^2 = X_{GSM}^2 + Z_{GSM}^2$  and  $Y_{EQ} = Y_{GSM}$ . For each bin in the equatorial plane and for each range of  $Kp$  and  $F_{10.7}$  index, we compute the median of the  $O^+$  and  $H^+$  density. The limitations of such mapping procedure are discussed in details by *Newell and Wing* [2000]. The main uncertainties and errors result from the following:

1. The presence of nonisotropic populations like field-aligned ion beams. This should be avoided by the set of conditions on plasma isotropy.
2. Experimental errors in density determination. Particle detectors are subject to significant error measurements even if they are carefully calibrated. CODIF data can contain false or unrealistic density values which may satisfy the imposed selection criteria, for instance, when the experiment is saturated or oppositely when the counting rates are two low. The choice of the median instead of the mean to compute the 1 min density aims to remove the effect of such unrealistic density values.
3. The use of a statistical magnetic field model like T96 also introduces limitations, in particular during perturbed periods when statistical models may fail to describe precisely the dynamic reconfigurations of the tail magnetic field. However, very active periods ( $Kp > 7$ ) when the uncertainty due to mapping is expected to be the highest are not included in our study. In the nightside magnetotail at distances between  $\sim 6$  and  $10 R_E$ , the estimated accuracy of the T96 model is better than  $1^\circ$  in latitude [*Shevchenko et al.*, 2010]. According to *Shevchenko et al.* [2010], the T96 model performs better than the older T89 model for which the mapping error from the ionospheric level to the magnetospheric equator at magnetic latitudes lower than  $69^\circ$  has been estimated to less than  $1 R_E$  by *Pulkkinen and Tsyganenko* [1996]. The Cluster spacecraft orbit at relatively high altitudes (higher than  $4 R_E$ ). We do not map the densities along the whole field lines which reduce the error due to mapping comparatively to such estimates made between the ionosphere and the magnetospheric equatorial plane.
4. The transport time between the ionosphere and the plasma sheet can vary between some minutes and some hours depending on several parameters like the location of the source region, the ion velocity, or the convection velocity. Consequently, the delay between the time we measure ions in the plasma sheet and the time they escaped the ionosphere is not taken into account. This prevents us from doing a precise timing analysis between variations of geomagnetic and solar activity and density changes in the plasma sheet. We thus limit our analysis to the average plasma sheet properties using indexes that describe the average geomagnetic activity level and solar EUV flux rather than indexes describing their variations at small timescales.
5. The use of the 3 h averaged  $Kp$  index as a proxy of geomagnetic activity. It is an indicator of the global geomagnetic activity level but does not account for processes occurring at small spatial scales or for the magnetospheric dynamic at short timescales.
6. The use of the daily  $F_{10.7}$  radio index as a proxy of the solar EUV flux. The  $F_{10.7}$  index is not a direct measurement of the solar EUV flux and does not account for possible delays in the ionospheric response to changes of the solar EUV flux level.

These limitations generate errors on both the density and the region of the equatorial plasma sheet where these densities are mapped. However, they should not limit our analysis as we focus on the ion density distribution on large scales.

### 2.3. Comparison With In Situ Data

To confirm the validity of the mapping technique, we first compare the results using our mapping technique with the results of *Mouikis et al.* [2010], who made a detail analysis of the composition of the midtail plasma sheet at geocentric distances between  $15$  and  $20 R_E$ . *Mouikis et al.* [2010] used CODIF partial densities between  $1$  and  $40$  keV from Cluster SC4 from 2001 to 2005 during the "tail seasons" (July to end of October) and restrained to measurement taken inside the central plasma sheet. We can thus compare these in situ observations with the result obtained from our mapping technique.

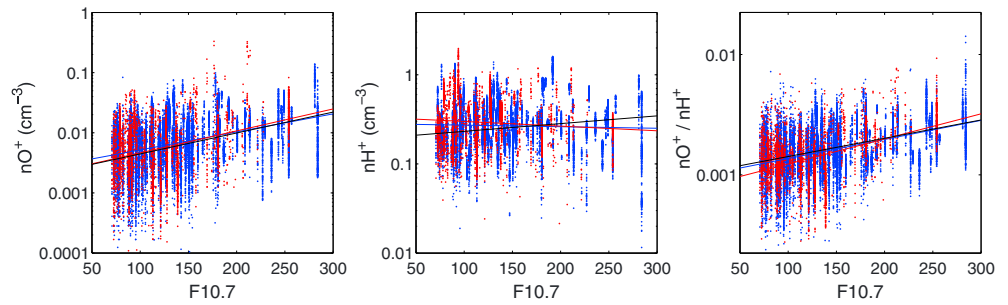


**Figure 1.** Scatterplot and fit of the  $F_{10.7}$  dependence of (left) the  $O^+$  density, (middle) the  $H^+$  density, and (right) the  $O^+$  to  $H^+$  density ratio during periods of low geomagnetic activity ( $K_p \leq 2$ ) in the midtail region. Densities measured inside the central plasma sheet are represented in red and densities measured in regions outside of but mapping into the central tail plasma sheet in blue. The black lines show the fitting curves obtained by *Mouikis et al.* [2010].

Figures 1 and 2 show scatterplots of the  $H^+$  and  $O^+$  densities as well as of the  $O^+/H^+$  density ratio in the midtail region as defined by *Mouikis et al.* [2010], respectively as a function of solar EUV flux and geomagnetic activity. Each point represents a 1 min median density value. Data have been sorted into two categories. The blue points correspond to measurements taken near the equatorial plane inside the region analyzed by *Mouikis et al.* [2010] while the red points correspond to measurements taken outside, at lower geocentric distances, but on magnetic field lines mapping into this region. The blue and red solid lines represent the corresponding linear regression fits of the logarithm of the densities and density ratio as a function of  $F_{10.7}$  or

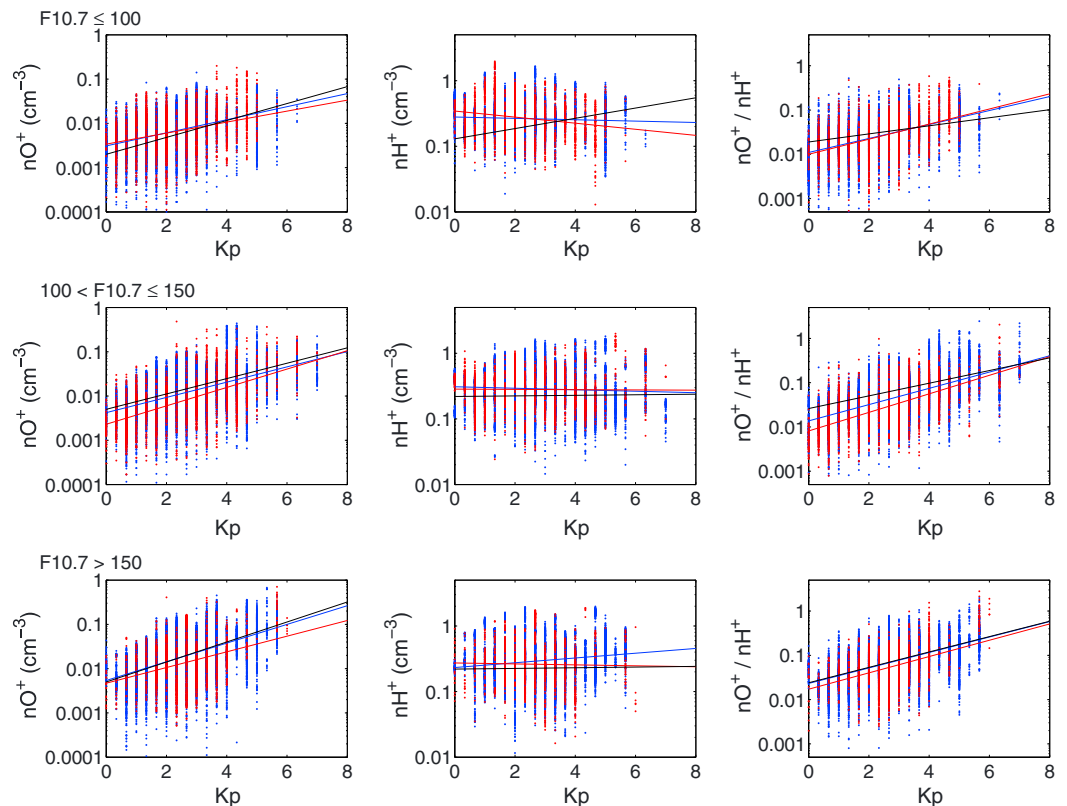


**Figure 2.** Scatterplot and fit of the  $K_p$  dependence of (left) the  $O^+$  density, (center) the  $H^+$  density, and (right) the  $O^+$  to  $H^+$  density ratio in the midtail region. From top to bottom: for  $F_{10.7} \leq 100$ , for  $100 < F_{10.7} \leq 150$ , and for  $F_{10.7} > 150$ . Densities measured inside the central plasma sheet are represented in red and densities measured in regions outside of but mapping into the central tail plasma sheet in blue. The black lines show the fitting curves obtained by *Mouikis et al.* [2010] for similar solar EUV levels.

**Table 1.** Regression Parameters ( $A$  and  $B$ ), Correlation Coefficient ( $R$ ), Number of Data Points ( $N$ ), and Correlation Significance Level of the  $F_{10.7}$  Dependence of the  $O^+$  Density,  $H^+$  Density, and  $O^+/H^+$  Density Ratio in the Midtail Region During Periods of Low Geomagnetic Activity ( $Kp \leq 2$ )<sup>a</sup>

	$A$	$B$	$R$	$N$	Correlation Significance
$nO^+ = A \times \exp(B \times F_{10.7})$					
IN	0.0025	0.0066	0.347	19,984	99.9%
OUT	0.0022	0.0067	0.278	3,730	99.9%
ALL	0.0024	0.0067	0.341	23,714	99.9%
$nH^+ = A \times \exp(B \times F_{10.7})$					
IN	0.26	-0.000092	0.008	19,984	70–80%
OUT	0.29	-0.00051	0.036	3,730	96–98%
ALL	0.26	-0.00019	0.016	23,714	98–99%
$nO^+/nH^+ = A \times \exp(B \times F_{10.7})$					
IN	0.0098	0.0066	0.394	19,984	99.9%
OUT	0.0078	0.0072	0.349	3,730	99.9%
ALL	0.0093	0.0069	0.395	23,714	99.9%

<sup>a</sup>The coefficients obtained for data taken inside (IN) and outside (OUT) the region analyzed by *Mouikis et al.* [2010] as well as the coefficient for all data points (ALL) are given.

$Kp$ , while the fits obtained by *Mouikis et al.* [2010] are plotted in black. The data have been selected using the same criteria as those used to produce the maps except for the  $Kp$  dependence (Figure 2) for which data have been sorted for three ranges of  $F_{10.7}$  ( $F_{10.7} \leq 100$ ,  $100 < F_{10.7} \leq 150$ , and  $F_{10.7} > 150$ ) to isolate comparable solar EUV flux. The results of the fit including the coefficients of the exponential function obtained by fitting the data and the corresponding correlation coefficients are listed in Table 1 ( $F_{10.7}$  dependence) and Table 2 ( $Kp$  dependence).

Data taken near the equatorial plane and data taken far from it show a comparable behavior both for the  $Kp$  and  $F_{10.7}$  dependence. Our results are also in good agreement with those of *Mouikis et al.* [2010]. In particular, we get a similar coefficient for the functional form obtained by fitting the density as a function of  $Kp$  and  $F_{10.7}$ . This confirms experimentally that the theoretical considerations and the assumptions we made to project the densities in the equatorial plane are valid.

### 3. Equatorial Maps

The two-dimensional density maps in the ( $X_{EQ}$ ,  $Y_{EQ}$ ) plane for  $O^+$  and  $H^+$  have been computed for different ranges of geomagnetic activity and solar EUV flux (Figures 3 and 4). The Sun is located on the right, and regions without data are colored in black.

Figure 3 shows the result for low ( $F_{10.7} \leq 100$ ), medium ( $120 < F_{10.7} \leq 150$ ), and high ( $F_{10.7} > 150$ ) solar EUV flux levels. Only periods of low geomagnetic activity ( $Kp \leq 2$ ) are considered. Figure 3a displays the median  $O^+$  density and Figure 3b the median  $H^+$  density. It shows that the  $H^+$  density does not vary significantly with solar EUV flux. Consequently, the spatial distribution of the  $O^+$  density and of the  $O^+$  to  $H^+$  density ratio displays a similar behavior. Like the  $H^+$  density, the  $O^+$  density is higher at low geocentric distances, but in contrast to the  $H^+$  density, the  $O^+$  density appears to be correlated with solar EUV flux. For low solar EUV flux, it is relatively low in the tail, and significant proportions of  $O^+$  ions are only observed in the very near Earth region. As solar EUV flux increases, the  $O^+$  density in the near-Earth region increases. For high  $F_{10.7}$  values and at low geocentric distances the  $O^+$  density is comparable with, though slightly lower than, the  $H^+$  density despite the low geomagnetic activity level. Furthermore, the region where the contribution of  $O^+$  ions is higher than a few percent expands, from geocentric distances lower than  $\sim 8 R_E$  for low solar EUV flux level to more than  $10 R_E$  for high solar EUV flux level. In contrast, farther in the tail the  $O^+$  density only slightly increases with solar EUV flux, and the  $O^+$  to  $H^+$  density ratio does not exceed  $\sim 0.05$  in this region.

Figure 4 shows in the same format as Figure 3 the  $O^+$  and  $H^+$  densities, for low ( $Kp \leq 2$ ), medium ( $2 < Kp \leq 4$ ), and high ( $Kp > 4$ ) geomagnetic activity levels. In order to keep a sufficient number of data points, in particular for high geomagnetic activity level, these maps include all solar EUV flux levels.

**Table 2.** Regression Parameters of the  $Kp$  Dependence of the  $O^+$  Density,  $H^+$  Density, and  $O^+/H^+$  Density Ratio in the Midtail Region for Three Solar EUV Flux Levels: Low ( $F_{10.7} \leq 100$ ), Medium ( $100 < F_{10.7} \leq 150$ ), and High ( $F_{10.7} > 150$ )<sup>a</sup>

		A	B	R	N	Correlation Significance
$nO^+ = A \times \exp(B \times Kp)$						
$F_{10.7}$ Low	IN	0.0028	0.35	0.431	11,610	99.9%
	OUT	0.0033	0.26	0.269	2,899	99.9%
	ALL	0.0029	0.33	0.393	14,509	99.9%
$F_{10.7}$ Med	IN	0.0040	0.40	0.495	16,867	99.9%
	OUT	0.0020	0.51	0.561	2,876	99.9%
	ALL	0.0035	0.42	0.511	19,743	99.9%
$F_{10.7}$ Hig	IN	0.0051	0.49	0.536	16,205	99.9%
	OUT	0.0036	0.46	0.321	2,160	99.9%
	ALL	0.0049	0.49	0.505	18,365	99.9%
$nH^+ = A \times \exp(B \times Kp)$						
$F_{10.7}$ Low	IN	0.25	-0.00042	0.0010	11,610	70–80%
	OUT	0.30	-0.080	0.143	2,899	99.9%
	ALL	0.26	-0.018	0.038	14,509	99.9%
$F_{10.7}$ Med	IN	0.29	-0.017	0.035	16,867	99.9%
	OUT	0.27	-0.0062	0.014	2,876	50–60%
	ALL	0.29	-0.014	0.031	19,743	99.9%
$F_{10.7}$ Hig	IN	0.23	0.086	0.156	16,205	99.9%
	OUT	0.23	0.033	0.044	2,160	95–96%
	ALL	0.23	0.082	0.144	18,365	99.9%
$nO^+/nH^+ = A \times \exp(B \times Kp)$						
$F_{10.7}$ Low	IN	0.011	0.35	0.486	11,610	99.9%
	OUT	0.011	0.34	0.411	2,899	99.9%
	ALL	0.011	0.35	0.469	14,509	99.9%
$F_{10.7}$ Med	IN	0.014	0.41	0.543	16,867	99.9%
	OUT	0.0073	0.52	0.639	2,876	99.9%
	ALL	0.012	0.44	0.5644	19,743	99.9%
$F_{10.7}$ Hig	IN	0.023	0.41	0.544	16,205	99.9%
	OUT	0.015	0.42	0.383	2,160	99.9%
	ALL	0.022	0.41	0.520	18,365	99.9%

<sup>a</sup>For each  $F_{10.7}$  range, the coefficients obtained for data taken inside (IN) and outside (OUT) the region analyzed by Mouikis et al. [2011] as well as the coefficient for all data points (ALL) are given.

No significant change of the  $H^+$  density distribution as a function of geomagnetic activity is observed. In contrast, the  $O^+$  density strongly depends on geomagnetic activity. It increases with increasing geomagnetic activity both in the midtail/far tail and at low geocentric distances. During quiet periods, a significant amount of  $O^+$  ions is detected only at low geocentric distances, below  $\sim 8\text{--}10 R_E$  where the ratio between  $O^+$  and  $H^+$  density can be higher than  $\sim 0.1$ . At higher geocentric distances, both in the dayside, on the flanks and in the nightside, the proportion of  $O^+$  ions represents only of a few percent of the total number density. During periods of moderate activity, the proportion of  $O^+$  ions is increased everywhere in the magnetosphere. The boundary of the near-Earth region rich in oxygen is less steep. In the near-Earth regions, the  $O^+/H^+$  density ratio approaches  $\sim 0.5$ , while in the midtail/far tail it is around 0.05. Finally, during periods of high geomagnetic activity the proportion of  $O^+$  ions is high everywhere in the magnetosphere, both in the near-Earth region where the  $O^+$  density can be comparable to the  $H^+$  density and in the tail where the density ratio reaches  $\sim 0.1$ .

Figures 3d and 4d display the relative standard deviation of the density ratio, i.e., the standard deviation of  $nO^+/nH^+$  divided by the median value of  $nO^+/nH^+$ . It is relatively high, around 1 in most regions. The high variability of the  $O^+$  to  $H^+$  density ratio is not surprising as our statistical approach does not account for small-scale spatial inhomogeneities and short timescale fluctuations of the  $O^+$  and  $H^+$  densities. Furthermore, densities are sorted only with respect to  $Kp$  and  $F_{10.7}$ , while ionospheric ion outflows and the magnetospheric plasma density and composition are expected to depend on several parameters including the solar wind dynamic pressure, the solar wind electric field, the interplanetary magnetic field (IMF) orientation, and its variability during the preceding hours [e.g., Cully et al., 2003a].

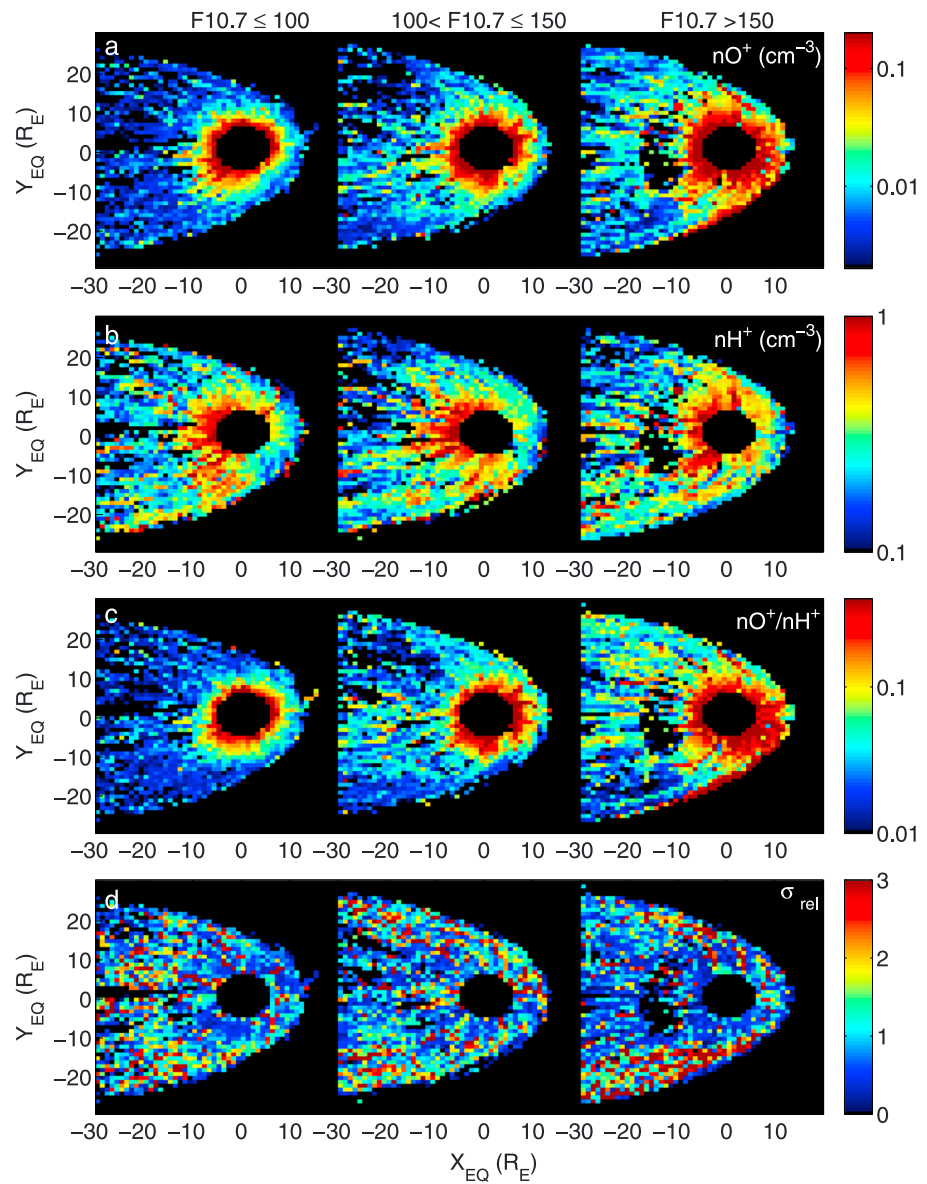


**Figure 3.** Two-dimensional maps in the magnetospheric equatorial plane during periods of low geomagnetic activity ( $Kp \leq 2$ ) for three ranges of  $F_{10.7}$  index: (left)  $F_{10.7} \leq 100$ , (middle)  $100 < F_{10.7} \leq 150$ , and (right)  $F_{10.7} > 150$ . (a)  $O^+$  ions number density, (b)  $H^+$  ions number density, (c)  $O^+/H^+$  density ratio, and (d) relative standard deviation of the  $O^+/H^+$  density ratio. The maps display the  $O^+$  density,  $H^+$  density, and  $O^+/H^+$  density ratio median value in each  $1 R_E \times 1 R_E$  bin.

The computed standard deviation is higher in the magnetospheric flanks and particularly for low  $Kp$  values. A detailed analysis of Cluster data in these regions of high variability suggests that two factors can contribute to it. The first is related to periods of low solar wind pressure. During such periods, the magnetosphere expands and with it, the inner magnetospheric regions rich in oxygen. Regions located close to the edge of this  $O^+$ -rich region can be located either inside or outside it depending on whether the solar wind pressure is low or high and thus are associated with highly variable  $O^+$  density. This is consistent with the fact that the standard deviation is higher during quiet periods when the  $O^+/H^+$  density ratio difference between inner and outer magnetosphere is steeper than during active periods.

The second reason is related to increased solar wind  $H^+$  entry of magnetosheath plasma in the magnetospheric flanks under predominantly northward IMF [e.g., Terasawa et al., 1997; Fujimoto et al.,

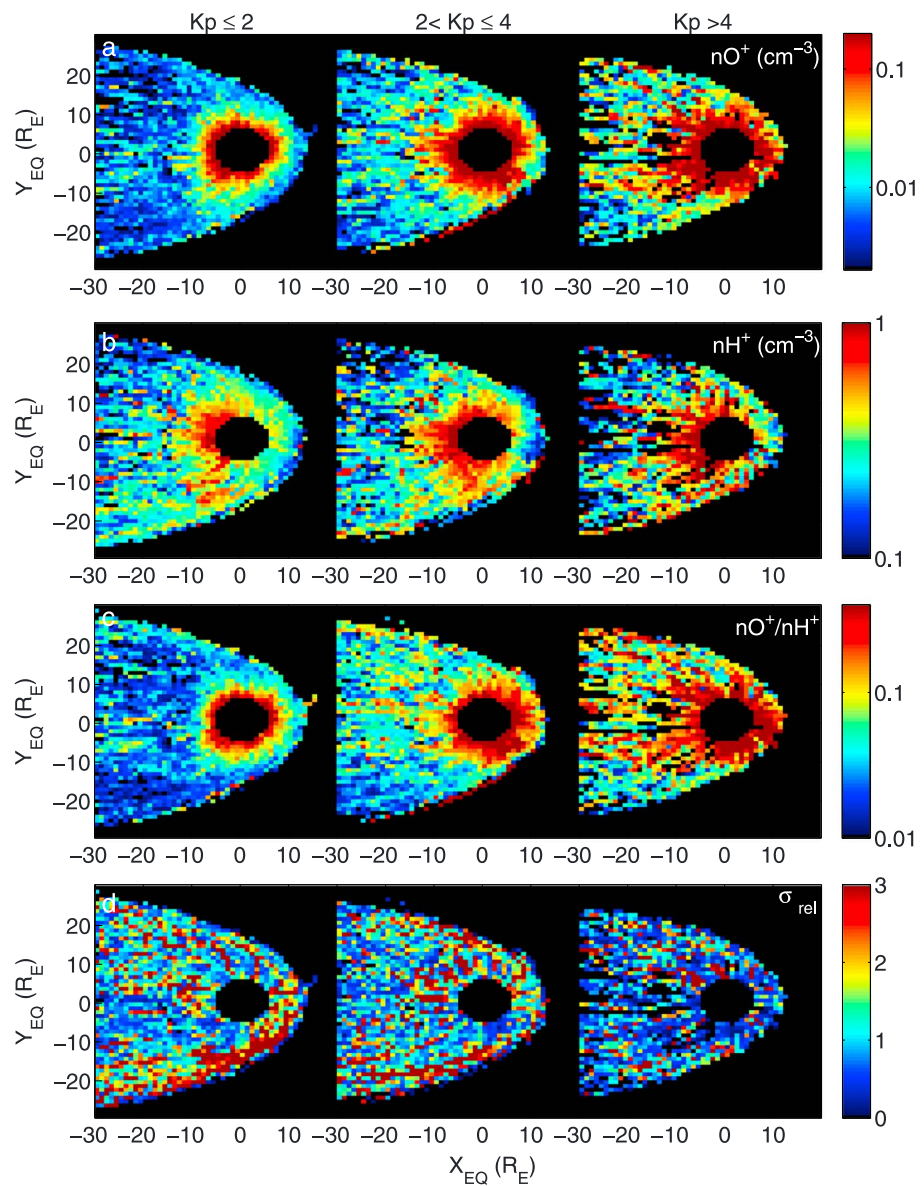


**Figure 4.** Two-dimensional maps in the magnetospheric equatorial plane for three ranges of  $Kp$  index: (left)  $Kp \leq 2$ , (middle)  $2 < Kp \leq 4$ , and (right)  $Kp > 4$ . All solar EUV flux levels are included. (a)  $O^+$  ions number density, (b)  $H^+$  ions number density, (c)  $O^+/H^+$  density ratio, and (d) relative standard deviation of the  $O^+/H^+$  density ratio. The maps display the  $O^+$  density,  $H^+$  density, and  $O^+/H^+$  density ratio median value in each  $1 R_E \times 1 R_E$  bin.

1998]. This may contribute to the fluctuations of the  $O^+$  to  $H^+$  density ratio observed in the dawn magnetospheric flank for all conditions except for high  $Kp$  values when the IMF is less likely to be northward oriented.

Both mechanisms are also consistent with the fact that the standard deviation is higher in the dawn flanks. Indeed, multifluid simulations suggest an asymmetric expansion of the magnetosphere—higher in the dawn sector than in the dusk sector—during periods of low solar wind pressure [Nishino et al., 2005], and observations by the DMSP satellite suggest that the solar wind entry processes are favored in the dawn flank [Wing et al., 2005].

In section 5 we will analyze in more detail the profile of the  $O^+$  and  $H^+$  density along the  $X_{EQ}$  axis, along the  $Y_{EQ}$  axis in the midtail, and as a function of magnetic local time (MLT) at low geocentric distances.

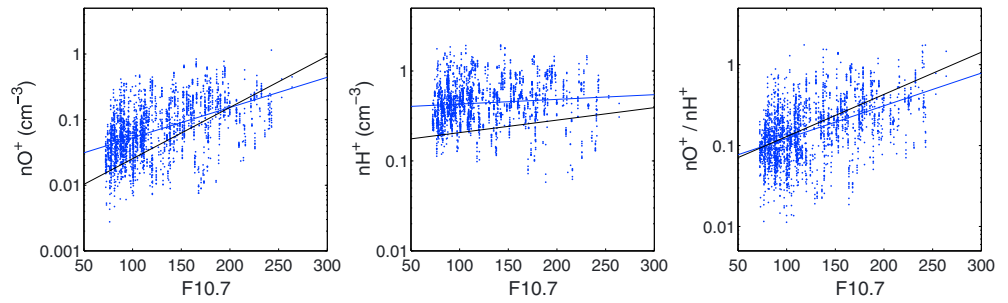


**Figure 5.** Scatterplot and fit of the  $F_{10.7}$  dependence of (left) the  $O^+$  density, (middle) the  $H^+$  density, and (right) the  $O^+$  to  $H^+$  density ratio during periods of low geomagnetic activity ( $Kp \leq 2$ ) in the near-Earth region. The black lines show the fitting curves obtained by Young *et al.* [1982] for the same range of  $Kp$  values.

#### 4. Detailed Analysis of the Midtail (15–20 $R_E$ ) and Near-Earth (7–8 $R_E$ ) Regions

The maps point out a distinct difference between the near-Earth regions where the proportion of  $O^+$  ions depends on both geomagnetic and solar activity level and the midtail/far tail regions where the main driver is geomagnetic activity. In this section we make a detailed analysis of the  $O^+$  and  $H^+$  density in these two regions.

The dependence of the  $O^+$  and  $H^+$  density on solar EUV flux during periods of low geomagnetic activity ( $Kp \leq 2$ ) and on geomagnetic activity in the midtail region is displayed in Figures 1 and 2 respectively. The coefficients of the corresponding exponential functional form of the density and density ratio as a function of  $F_{10.7}$  and  $Kp$  are given in Tables 1 and 2 respectively. The dispersion of data about the mean for a given  $F_{10.7}$  or  $Kp$  value is relatively high, about 1 order of magnitude, both for the  $O^+$  density and the  $H^+$  density. The density ratio also shows a large variability which indicates that the source of this variance is not common for the two species.

In the midtail region, the  $O^+$  density and  $O^+/H^+$  density ratio are clearly correlated with  $F_{10.7}$ . On the contrary, the  $H^+$  density is not correlated with  $F_{10.7}$ . It is almost constant whatever the solar EUV flux level is. Consequently, the  $O^+$  density and  $O^+/H^+$  density ratio have similar dependence on the  $F_{10.7}$  index. From low  $F_{10.7}$  values (70) to high  $F_{10.7}$  values (250) they increase by a factor of  $\sim 3.5$ .

For high solar EUV flux the  $H^+$  density appears to increase slightly with increasing geomagnetic activity, while for medium solar EUV flux levels it is almost constant. However, the correlation coefficients and the density variations are weak which indicate that the  $H^+$  density may not be—or very weakly—correlated with geomagnetic activity. Conversely, there is a strong correlation between the geomagnetic activity and the  $O^+$  density and  $O^+/H^+$  density ratio. From low to high geomagnetic activity the  $O^+$  density and the  $O^+/H^+$  density ratio strongly increase. This increase depends on the range of  $F_{10.7}$  index, i.e., on the solar EUV flux level and thus on the phase of the solar cycle. It is significantly higher during periods when the solar EUV flux is high. When the  $Kp$  index increases from 0 to 7, the  $O^+$  density increases on average by a factor of  $\sim 10$  for low ( $F_{10.7} \leq 100$ ) and of  $\sim 19$  for medium ( $100 < F_{10.7} \leq 150$ ) solar EUV flux, while for high solar EUV flux ( $F_{10.7} > 150$ ) it increases by a factor of  $\sim 31$ . The increase of the  $O^+/H^+$  density ratio is on average of  $\sim 12$ ,  $\sim 22$ , and  $\sim 18$  respectively for low, medium, and high  $F_{10.7}$  levels.

A multiple regression fit has been made to provide functional forms describing the density variation as a function of  $F_{10.7}$  and  $Kp$  in the midtail region:

$$nO^+ = 0.0014 \exp(0.00072 F_{10.7} + 0.44 Kp) \text{ cm}^{-3} \quad (1)$$

$$R_{F_{10.7}} = 0.30 \quad R_{Kp} = 0.49$$

$$nH^+ = 0.23 \exp(0.00069 F_{10.7} + 0.0020 Kp) \text{ cm}^{-3} \quad (2)$$

$$R_{F_{10.7}} = 0.051 \quad R_{Kp} = 0.042$$

$$nO^+/nH^+ = 0.0058 \exp(0.0065 F_{10.7} + 0.42 Kp) \text{ cm}^{-3} \quad (3)$$

$$R_{F_{10.7}} = 0.31 \quad R_{Kp} = 0.53$$

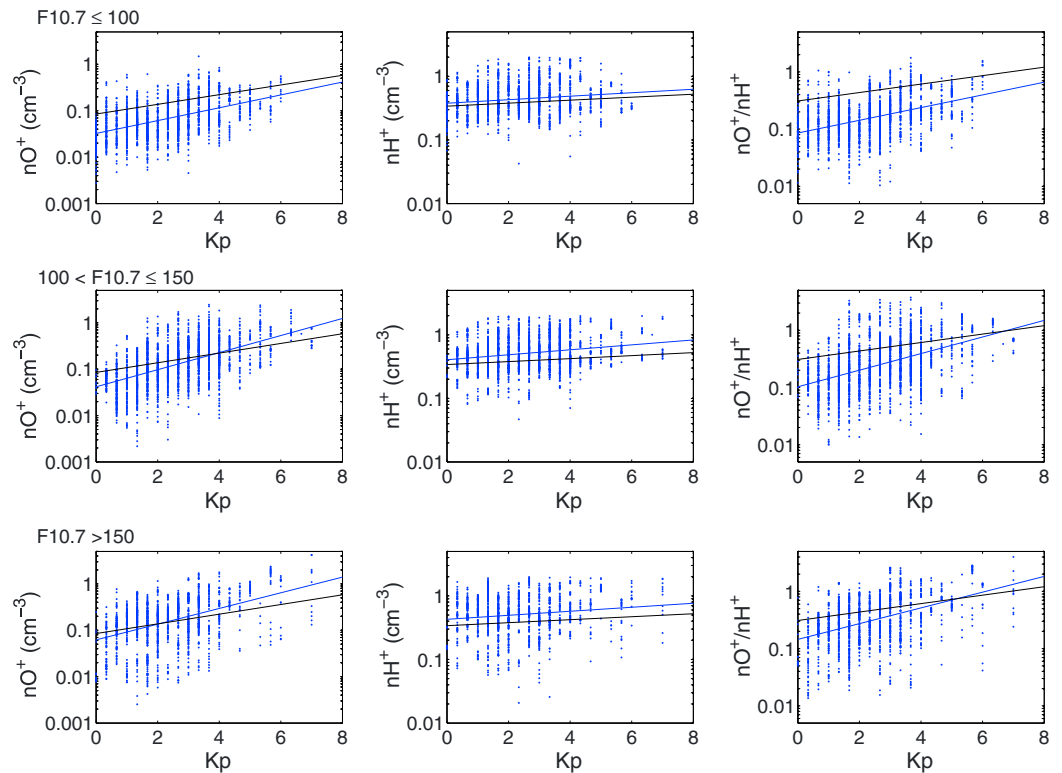


**Figure 6.** Scatterplot and fit of the  $K_p$  dependence of (left) the  $O^+$  density, (middle) the  $H^+$  density, and (right) the  $O^+$  to  $H^+$  density ratio in the near-Earth region. From top to bottom: for  $F_{10.7} \leq 100$ , for  $100 < F_{10.7} \leq 150$ , and for  $F_{10.7} > 150$ . The black lines show the fitting curves obtained by *Young et al.* [1989].

where  $R_{F_{10.7}}$  and  $R_{K_p}$  are the correlation coefficients obtained from the multiple regression analysis. For  $nO^+$  and  $nO^+/nH^+$  they indicate a statistically significant correlation with  $F_{10.7}$  and  $K_p$ . For  $nH^+$  the very low value of  $R_{F_{10.7}}$  and  $R_{K_p}$  means that the correlation with  $K_p$  and  $F_{10.7}$  is not statistically significant. These functional forms provide variation rates similar to what has been obtained by considering the  $F_{10.7}$  and  $K_p$  variables alone (see Tables 1 and 2).

We made a similar analysis at lower geocentric distances. Figures 5 and 6 display scatterplots of the  $H^+$  and  $O^+$  densities as well as of the  $O^+/H^+$  density ratio respectively as a function of solar EUV flux during periods of low geomagnetic activity ( $K_p \leq 2$ ) and of geomagnetic activity in the same format as Figures 1 and 2. They include all density measurements taken in regions mapping in the equatorial plane at distances between  $7 R_E$  and  $8 R_E$  (to avoid at best the radiation belts) irrespective of the MLT. The linear fit of the logarithm of the density and density ratio is represented by a blue line, while the linear fit obtained by *Young et al.* [1982] from the analysis of density measurements from the GOES spacecraft for a comparable energy range (from 0.9 to 15.9 keV) near geocentric orbit is plotted in black. The coefficients of the corresponding

**Table 3.** Regression Parameters of the  $F_{10.7}$  Dependence of the  $O^+$  Density,  $H^+$  Density, and  $O^+/H^+$  Density Ratio in the Near-Earth Region During Periods of Low Geomagnetic Activity ( $K_p \leq 2$ )

A	B	R	N	Correlation Significance
		$nO^+ = A \times \exp(B \times F_{10.7})$		
0.017	0.012	0.503	3129	99.9%
		$nH^+ = A \times \exp(B \times F_{10.7})$		
0.33	0.0024	0.190	3129	99.9%
		$nO^+/nH^+ = A \times \exp(B \times F_{10.7})$		
0.052	0.0092	0.449	3129	99.9%

**Table 4.** Regression Parameters of the  $Kp$  Dependence of the  $O^+$  Density,  $H^+$  Density, and  $O^+/H^+$  Density Ratio in the Near-Earth Region for Three Solar EUV Flux Levels: Low ( $F_{10.7} \leq 100$ ), Medium ( $100 < F_{10.7} \leq 150$ ), and High ( $F_{10.7} > 150$ )

	A	B	R	N	Correlation Significance
$nO^+ = A \times \exp(B \times Kp)$					
$F_{10.7}$ Low	0.034	0.29	0.426	2410	99.9%
$F_{10.7}$ Med	0.049	0.37	0.511	2599	99.9%
$F_{10.7}$ Hig	0.086	0.31	0.401	1724	99.9%
$nH^+ = A \times \exp(B \times Kp)$					
$F_{10.7}$ Low	0.36	0.070	0.180	2410	99.9%
$F_{10.7}$ Med	0.41	0.086	0.208	2599	99.9%
$F_{10.7}$ Hig	0.45	0.060	0.131	1724	99.9%
$nO^+/nH^+ = A \times \exp(B \times Kp)$					
$F_{10.7}$ Low	0.094	0.22	0.375	2410	99.9%
$F_{10.7}$ Med	0.12	0.28	0.420	2599	99.9%
$F_{10.7}$ Hig	0.19	0.25	0.367	1724	99.9%

exponential functional form of the density and density ratio as a function of  $F_{10.7}$  and  $Kp$  are given in Tables 3 and 4 respectively.

As for the midtail region, the dispersion of data is of about 1 order of magnitude both for the  $O^+$  density,  $H^+$  density, and  $O^+/H^+$  density ratio.

We find a weak but statistically significant correlation between the  $H^+$  density and  $Kp$ . It corresponds to a small increase of the  $H^+$  density with geomagnetic activity by respectively 60% (low  $F_{10.7}$ ), 80% (medium  $F_{10.7}$ ), and 50% (high  $F_{10.7}$ ) over the full range of  $Kp$  from 0 to 7. Similarly, we find a weak but statistically significant correlation between the  $H^+$  density and the  $F_{10.7}$  index, the amount of  $H^+$  being about 50% higher for high solar EUV flux levels ( $F_{10.7} = 250$ ) compared to low solar EUV flux levels ( $F_{10.7} = 70$ ).

Like in the tail region, at low geocentric distances, the  $O^+$  density and  $O^+/H^+$  density ratio are also correlated with geomagnetic activity and solar EUV flux. Similarly, the amount of  $O^+$  ions increases with solar EUV flux and geomagnetic activity. However, there are two noteworthy differences between these two regions. In the near-Earth regions the  $O^+$  density and  $O^+/H^+$  density increase at a lower rate with geomagnetic activity, and this increase does not seem to be related to the solar EUV flux level. When  $Kp$  increases from 0 to 7, the  $O^+$  density increases by a factor of  $\sim 8$  for low solar EUV flux levels, of  $\sim 13$  for medium solar EUV flux levels, and of  $\sim 9$  for high solar EUV flux levels. On average, the increase of the  $O^+/H^+$  density ratio is of  $\sim 5$ ,  $\sim 7$ , and  $\sim 6$  respectively for low, medium, and high  $F_{10.7}$  levels.

Another striking feature of the near-Earth regions is the strong effect of solar EUV flux on the  $O^+$  density during quiet periods. For an increase of  $F_{10.7}$  from 70 to 250, the  $O^+$  density and  $O^+/H^+$  density ratio increase respectively of a factor of  $\sim 7$  and  $\sim 5$  which is about 2 times higher than in the tail.

These results are in relatively good agreement with the findings by *Young et al.* [1982] although they report a slightly higher increase rate of the  $O^+$  density with solar EUV flux but a lower increase rate with geomagnetic activity and lower  $H^+$  densities. These differences may result from the differences between the Cluster and GOES particle detectors (in particular their energy range) and to the fact that we consider slightly higher geocentric distances.

A multiple regression analysis provides functional forms describing the density variation as a function of  $F_{10.7}$  and  $Kp$  in the near-Earth region:

$$nO^+ = 0.016 \exp(0.0092 F_{10.7} + 0.32 Kp) \text{ cm}^{-3} \quad (4)$$

$$R_{F_{10.7}} = 0.396 \quad R_{Kp} = 0.439$$

$$nH^+ = 0.33 \exp(0.0016 F_{10.7} + 0.073 Kp) \text{ cm}^{-3} \quad (5)$$

$$R_{F_{10.7}} = 0.129 \quad R_{Kp} = 0.185$$

$$nO^+/nH^+ = 0.049 \exp(0.0076 F_{10.7} + 0.24 Kp) \text{ cm}^{-3} \quad (6)$$

$$R_{F_{10.7}} = 0.370 \quad R_{Kp} = 0.384$$

The correlation coefficients  $R_{F_{10.7}}$  and  $R_{Kp}$  indicate that the correlation between these three quantities and  $Kp$  and  $F_{10.7}$  is statistically significant. We note that with the multiple regression analysis, which includes all  $Kp$  and  $F_{10.7}$  values, the variation of the densities as a function of  $F_{10.7}$  is less pronounced than when only quiet periods are considered (see Table 3). When all geomagnetic activity levels are considered, the increase of the  $O^+$  density and  $O^+/H^+$  density ratio from low to high solar EUV flux is respectively a factor of  $\sim 5$  and  $\sim 4$  while the  $H^+$  density is 30% higher for high solar EUV flux. A similar behavior has been reported observed by Young *et al.* [1982], with a slightly higher increase rate of the  $O^+$  density and of the  $O^+/H^+$  density ratio with solar EUV flux for periods of low geomagnetic activity.

## 5. Density Profiles

In this section we analyze the spatial profile of the  $O^+$  density,  $H^+$  density, and  $O^+/H^+$  density ratio for various  $F_{10.7}$  and  $Kp$  ranges in the tail and in the near-Earth regions.

In the previous sections we have shown that the dispersion of the densities and density ratio around the median value is large, about 1 order of magnitude. This dispersion is quantified by the standard deviation, which is of the same order of magnitude as the density and density ratio value. As discussed above, this variability can be either due to measurement errors or to the “natural” variability of the density. That all studies analyzing the magnetospheric  $O^+$  and  $H^+$  densities reported a similar variability [e.g., Young *et al.*, 1982; Mouikis *et al.*, 2010; Ohtani *et al.*, 2011], independent of the experiment or of the method used to process data suggests that the second one account for most of the dispersion of data.

Despite this high variability, we have shown that geomagnetic activity and solar EUV flux have an unambiguous effect on the  $O^+$  density and on the  $O^+/H^+$  density ratio. Indeed, while the variations of the median density and median density ratio over the full range of  $Kp$  and  $F_{10.7}$  are comparable to the standard deviation for a given value of  $Kp$  or  $F_{10.7}$ , the  $O^+$  density and the  $O^+/H^+$  density ratio are clearly correlated with  $Kp$  and  $F_{10.7}$ .

Analyzing the density and density ratio spatial profiles requires estimating the error in the determination of their median values. The standard deviation  $\sigma$  represents the spread of data around the mean value. For a Gaussian distribution the statistical uncertainty in the determination of the mean value (equivalent to the median value in that case) is given by the product between Student coefficients  $s_N$  and  $\sigma/\sqrt{N}$  where  $N$  is the number of samples. For a confidence level of 95%  $s_N$  is equal to 1.96 if the number of data points is large enough ( $>30$ ) which is the case for most of the data plotted in the spatial profiles.

This only stands for the statistical uncertainty in the determination of the mean value from a set of  $N$  measurements. It does not include other sources of uncertainty like measurement errors that are impossible to characterize accurately enough. Furthermore, we may not be dealing with Gaussian distributions. Despite these limitations, we will use this method to compute the error bars. However, the reader has to keep in mind that the actual error is higher if all the contributions are taken into account.

In the following figures, the error bars are larger for high  $Kp$  values. This is in large part due to the lower number of available data points for  $Kp > 4$ . However, the standard deviation is actually slightly higher for high  $Kp$  values compared to low and medium  $Kp$  values (on average  $\sim 5$  times higher for the  $O^+$  density and  $\sim 4$  times higher  $O^+/H^+$  density ratio). But as the  $O^+$  density is higher when  $Kp$  is high, the relative value of the standard deviation is almost constant (see Figure 3).

Figure 7 displays the profile of the  $H^+$  density,  $O^+$  density, and  $O^+/H^+$  density ratio in the magnetospheric tail ( $-20 R_E < X_{EQ} < -15 R_E$ ) as a function of  $Y_{EQ}$  respectively for three ranges of  $F_{10.7}$  ( $F_{10.7} \leq 100$ ,  $100 < F_{10.7} \leq 150$ , and  $F_{10.7} > 150$ ) and  $Kp$  ( $Kp \leq 2$ ,  $2 < Kp \leq 4$ , and  $Kp > 4$ ). This region corresponds to the midtail region analyzed in section 4. As expected, these figures emphasize the main features discussed in sections 3 and 4. The  $H^+$  density profile is similar for all ranges of  $Kp$  and  $F_{10.7}$  as expected from the weak correlation of the  $H^+$  density with  $Kp$  and  $F_{10.7}$ . On the contrary, the  $O^+$  density and  $O^+/H^+$  density ratio profiles vary more with geomagnetic activity than with solar EUV flux which is consistent with the strong influence of the geomagnetic activity compared to the solar EUV flux on the  $O^+$  content in this region. There is no noteworthy indication of a dependence of the  $O^+$  and  $H^+$  density and of the  $O^+/H^+$  density ratio on  $Y_{EQ}$

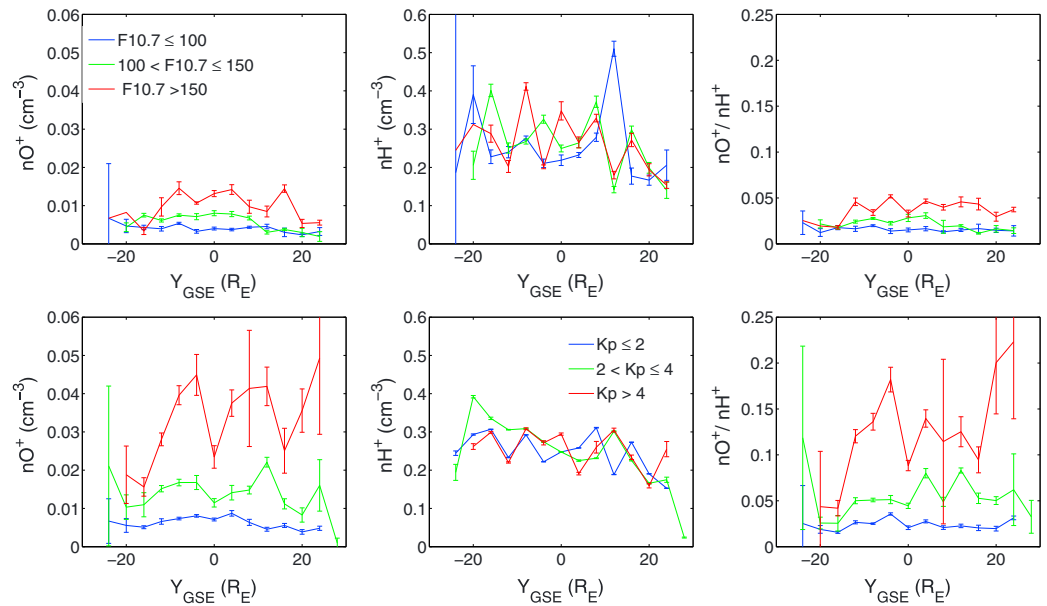


**Figure 7.** Profile along the  $Y_{EQ}$  axis of the (left)  $O^+$  density, (middle)  $H^+$  density, and (right)  $O^+$  to  $H^+$  density ratio during periods of low geomagnetic activity ( $Kp \leq 2$ ) (top) for three ranges of  $F_{10.7}$  index and (bottom) for three ranges of  $Kp$  index with no restriction on the solar EUV flux level. The data are averaged over regions between  $-20 R_E < X_{EQ} < -15 R_E$ .

whatever is the considered range of  $Kp$  or  $F_{10.7}$ . The observed variations are of the same order of magnitude as the error bars and are not structured but rather appear to be randomly distributed.

Figure 8 displays the profile of the  $H^+$  density,  $O^+$  density, and  $O^+/H^+$  density as a function of MLT in the near-Earth region at equatorial geocentric distances between  $7 R_E$  and  $8 R_E$  in the same format as Figure 7. According to results from section 4, the  $H^+$  density profile display a moderate increase with increasing geomagnetic and solar EUV flux levels. For low and medium  $Kp$  values, the  $H^+$  density in the 1–40 keV range peaks in

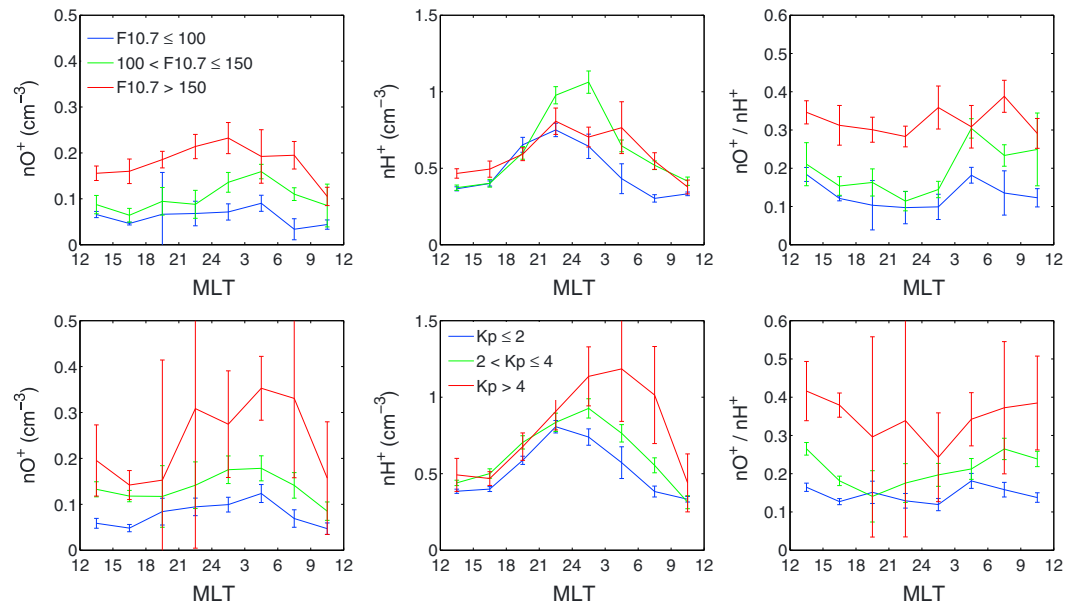


**Figure 8.** Profile as a function of MLT of the (left)  $O^+$  density, (middle)  $H^+$  density, and (right)  $O^+$  to  $H^+$  density ratio during periods of low geomagnetic activity ( $Kp \leq 2$ ) (top) for three ranges of  $F_{10.7}$  index and (bottom) for three ranges of  $Kp$  index with no restriction on the solar EUV flux level. The data are averaged over geocentric distances comprised between  $7 R_E$  and  $8 R_E$ .

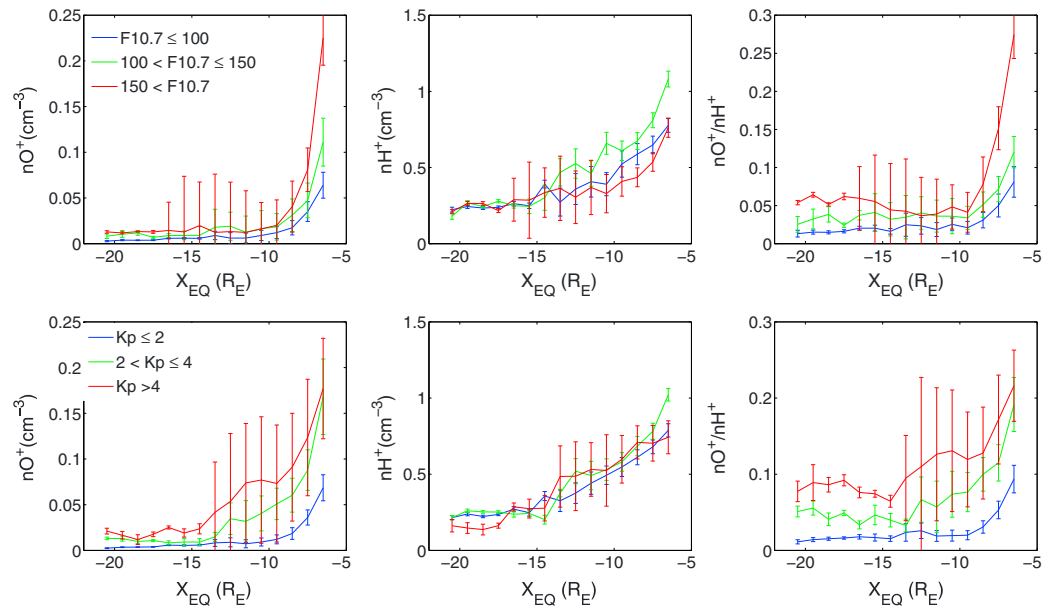


**Figure 9.** Profile along the  $X_{EQ}$  axis of the (left)  $O^+$  density, (middle)  $H^+$  density, and (right)  $O^+$  to  $H^+$  density ratio during periods of low geomagnetic activity ( $Kp \leq 2$ ) (top) for three ranges of  $F_{10.7}$  index and (bottom) for three ranges of  $Kp$  index with no restriction on the solar EUV flux level. The data are averaged over regions between  $-5 R_E < Y_{EQ} < 5 R_E$ .

the nightside region, and no clear dawn/dusk asymmetry is observed. However, for high  $Kp$  the peak is shifted to the morning side. The MLT distribution of the  $O^+$  density displays a similar behavior. Consequently, the  $O^+/H^+$  density ratio for energies between 1 and 40 keV is relatively uniform with no significant MLT dependence. Furthermore, the changes in the  $O^+$  density and  $O^+/H^+$  density profiles for different ranges of  $F_{10.7}$  and  $Kp$  are of a similar magnitude which further confirms that in the near-Earth region solar EUV flux and geomagnetic activity have comparable effect on the  $O^+$  content.

Figure 9 displays the profile of the  $H^+$  density,  $O^+$  density, and  $O^+/H^+$  density averaged over the region  $-5 R_E < Y_{EQ} < 5 R_E$  as a function of  $X_{EQ}$  respectively for three ranges of  $F_{10.7}$  ( $F_{10.7} \leq 100$ ,  $100 < F_{10.7} \leq 150$ , and  $F_{10.7} > 150$ ) and  $Kp$  ( $Kp \leq 2$ ,  $2 < Kp \leq 4$ , and  $Kp > 4$ ). The  $O^+$  and  $H^+$  densities decrease with increasing distance from the Earth irrespective of the geomagnetic activity and solar EUV flux. The  $H^+$  density decreases smoothly with geocentric distance, and there is no major change of the  $H^+$  profile with the geomagnetic activity and solar EUV flux level. Consistent with the observations reported in sections 3 and 4, the  $O^+$  density profile displays distinct behavior at low and high geocentric distances. In particular, the  $O^+$  density and  $O^+/H^+$  density ratio increase with decreasing geocentric distance is steeper for high  $F_{10.7}$  which is consistent with the fact that they increase at a higher rate with increasing solar EUV flux in the near-Earth region than farther in the tail. The strong influence of solar EUV flux at low geocentric distances is also evidenced by the fact that the average density for  $F_{10.7} > 150$  during quiet periods is higher than the average density for  $Kp > 4$  (which includes all solar EUV flux levels). However, these average profiles should not hide that the highest amount of  $O^+$  are observed during active periods even if the solar EUV flux level is low (see Figures 5 and 6).

At geocentric distances higher than 8–10  $R_E$ , the decrease of the  $O^+$  density as a function of geocentric distance is less steep. At such distances, the solar EUV flux level has only a weak influence on the  $O^+$  density. The  $O^+$  density is weak during quiet periods but significantly increases with geomagnetic activity. At geocentric distances between 10 and 20  $R_E$ , the  $O^+$  and  $H^+$  densities decrease at a relatively similar rate, and consequently, the proportion of  $O^+$  ions is almost constant. Note that in these profiles, the uncertainty on the density values is much higher at geocentric distances lower than  $\sim 15 R_E$ . This is not due to an increase of the densities variability but actually results from the low number of data points available in this region located between Cluster apogee and perigee.

## 6. Discussion and Conclusion

This study provides a detailed picture of the 1–40 keV  $H^+$  and  $O^+$  ion distribution in the magnetospheric equatorial plane. It confirms that  $O^+$  ions represent a significant amount of the plasma sheet ions even at large geocentric distances.

We analyzed the dependence of the  $H^+$  and  $O^+$  ion density on geomagnetic activity and solar EUV flux. As expected, we show that the amount of  $O^+$  ions in the magnetosphere increases with increasing geomagnetic activity and solar EUV flux. However, despite the good correlation between the  $O^+$  density and the  $O^+/H^+$  density ratio with  $Kp$  and  $F_{10.7}$ , the  $O^+$ ,  $H^+$  densities as well as the  $O^+/H^+$  density ratio are highly variable. As observed for ionospheric outflows [e.g., Cully *et al.*, 2003a], the plasma sheet  $O^+$  density and  $O^+/H^+$  density ratio for a single measurement can deviate from predicted trends by more than 1 order of magnitude. Consequently, the fitting functions given in this paper can be used as indicators of the average values but are not expected to provide accurate predictive values.

Despite this high variability, clear trends as a function of solar EUV flux and geomagnetic activity and unambiguous distinct behavior between the near-Earth regions at distances lower than  $\sim 10 R_E$  and the midtail region at distances between  $\sim 15$  and  $20 R_E$  have been evidenced. The advantage of the mapping technique used in this study is that the plasma sheet density can be analyzed in its entirety. The data come from a single experiment and are taken during the same time period. This allows direct and unambiguous comparison between different magnetospheric regions and/or solar wind and solar EUV conditions. In contrast, comparing results from various studies is not straightforward. Indeed, the observed differences are likely to result from the experiments characteristics, from the methods and techniques used or from the time period when the analysis is made.

Comparison with previous published results shed light on this problem. The total ion density in this study is significantly lower (by a factor of  $\sim 2$  on average) than the total ion density reported by Wing and Newell [1998]. They used a similar mapping technique but extrapolated the full ion density from DMSP Special Sensor for Precipitating Particles (SSJ4) measurements (which cannot distinguish different ion species and does not measure the ion 3-D distribution) at low altitude ( $\sim 800$  km). Furthermore, the solar wind pressure was high during the interval they analyzed which may have increased the plasma sheet density. On the other hand, we obtain slightly higher densities than reported by Ohtani *et al.* [2011] who attempted to estimate the total  $O^+$  and  $H^+$  from Geotail density measurements between 9 and 210 keV. Contrary to previous observations but in agreement with Cluster in situ observations [Mouikis *et al.*, 2010], we do not observe a dawn-dusk asymmetry [Wing and Newell, 1998] or maxima located around  $Y_{GSM} = \pm 10 R_E$  [Lennartsson and Shelley, 1986] in the ion density profile along the  $Y_{EQ}$  axis. As suggested by Mouikis *et al.* [2010], this may result from the conditions we impose on the  $H^+$  density ( $nH^+ < 2 \text{ cm}^{-3}$ ) and on the ion energy ( $E > 1 \text{ keV}$ ) that may exclude the low-latitude boundary layer populations.

### 6.1. Implication on Ionospheric Outflow

The outflow rate is not the only factor modulating the plasma sheet density and composition. Ionospheric ions transport, and energization as well as plasma sheet loss rate also play a major role. Separating their contribution from the contribution of ionospheric sources, flux modulation by geomagnetic activity and solar EUV flux is not possible from measurements taken in the plasma sheet. We observe the final result of these processes but have no information on their relative impact. Nevertheless, our observations of the plasma sheet composition provide constraints on the ionospheric sources and on processes related to ionospheric ions outflow and transport. In particular, it can provide hints on the origin of the ionospheric  $O^+$  ions directly entering the plasma sheet in the near-Earth region.

This study confirms that the amount of  $O^+$  ions is higher at low geocentric distances. Furthermore, it shows that in the near-Earth regions the decrease of the  $O^+$  density with geocentric distance is steeper than for  $H^+$  ions and that the dependence of  $O^+$  density with  $Kp$  and  $F_{10.7}$  differs between low and high geocentric distances.

These differences further confirm that  $O^+$  ions directly enter the plasma sheet at low geocentric distances as previously suggested by, e.g., Lennartsson and Shelley [1986], Mouikis *et al.* [2010], and Ohtani *et al.* [2011] to account for the higher  $O^+$  density in the near-Earth plasma sheet. The increase of the proportion of  $O^+$  ions

from high to low geocentric distances is observed for all kinds of conditions which suggest that the direct entry of  $O^+$  ions in the near-Earth region is a permanent process. Note that the different behavior of the  $O^+$  density and  $O^+/H^+$  density ratio between near-Earth regions and the tail had been noticed by *Mouikis et al.* [2010] as they compared their observations to GOES measurements at geostationary orbit [*Young et al.*, 1982]. However, they could not exclude that it was resulting from the different energy ranges of the Cluster and GOES ion detectors.

The auroral region is a major source of energetic ionospheric ions and is magnetically connected to the near-Earth plasma sheet. Auroral outflow contains a significant amount of  $O^+$  ions [e.g., *Yau et al.*, 1985a, 1985b, 1988; *Yau and Andre*, 1997] and is thus a good candidate for providing  $O^+$  ions to the near-Earth regions ( $< 10 R_E$ ).

Extended statistical study of energetic outflow (0.01–17 keV) based on measurements from the DE 1 spacecraft [*Yau et al.*, 1988] reveals that energetic  $O^+$  outflows strongly increase with increasing geomagnetic activity (up to a factor of 20 from low to high geomagnetic activity) while the corresponding increase of  $H^+$  ion outflow is of about a factor of  $\sim 4$ . Solar EUV flux is associated with an increase of the  $O^+$  flux by a factor of  $\sim 5$  even in the nightside auroral zone [*Yau et al.*, 1985b] and with a statistically marginal decrease of the  $H^+$  flux over the full  $F_{10.7}$  range. Note that according to this study, 90% of auroral outflow measured by DE 1 consists in ions with energies below 1 keV.

Ions outflowing from the cusp and the polar regions are dispersed according to their velocity while they transit in the lobe region. Energetic ( $> 100$  eV)  $O^+$  ions outflowing from the cusp region are too fast to reach the plasma sheet at low geocentric distances [e.g., *Nilsson et al.*, 2012]. On the contrary, low-energy  $O^+$  ions have much lower velocities and may thus enter the plasma sheet at lower geocentric distances. Significant upward flux of low-energy  $O^+$  ions above the polar ionosphere has been observed by the DE 1 satellite [e.g., *Gurgiolo and Burch*, 1982; *Chandler*, 1995], the Akebono satellite [e.g., *Abe et al.*, 1993, 2004; *Cully et al.*, 2003a], and the Polar satellite [e.g., *Su et al.*, 1998; *Elliott et al.*, 2001]. Upward fluence up to  $10^{26}$   $O^+$  ions per second has been reported by *Cully et al.* [2003a]. Note that this estimate includes low-energy outflow from both the cusp, polar cap, and auroral regions as these sources cannot be easily separated by measurements taken above the high-latitude ionosphere [see *Yau and Andre*, 1997; *Peterson et al.*, 2008]. Using measurement from the Akebono satellite and particle trajectory tracing, *Kitamura et al.* [2010] showed that during geomagnetic storms,  $< 10$  eV  $O^+$  ions contribute significantly to populate the near-Earth tail region and ring current and *Cully et al.* [2003b] showed that a substantial amount of low-energy ( $< 20$  eV)  $O^+$  and  $H^+$  ions escaping from the polar ionosphere enters the plasma sheet at low geocentric distances ( $< 10 R_E$ ) even during quiet periods.

Consequently, low-energy ions from the cusp and polar ionosphere are also likely to contribute to the direct entry of  $O^+$  ions in the near-Earth plasma sheet.

The flux of low-energy outflowing ions increases with increasing geomagnetic activity and solar EUV flux levels [e.g., *Cully et al.*, 2003a; *Engwall et al.*, 2009; *Lennartsson et al.*, 2004]. Low-energy  $O^+$  outflow seems particularly sensitive to solar EUV flux. *Cully et al.* [2003a] in an extensive study of low-energy (1–70 eV)  $O^+$  and  $H^+$  outflows using measurements from the Akebono satellite at altitudes between 2000 and 10000 km reported an increase of the  $O^+$  flux by a factor of  $\sim 20$  from low to high solar EUV flux. Contrary to energetic  $H^+$  ions, low-energy  $H^+$  ions outflow also increase with increasing solar EUV flux while at a lower rate (by a factor of  $\sim 2$ –3 from low to high  $F_{10.7}$ ).

Neither energetic nor cold outflow variations with solar and geomagnetic activity correspond to the  $O^+$  and  $H^+$  density variations observed in the near-Earth plasma sheet, further evidencing the difficulty to make conclusions about the ionospheric sources from density measurements in the plasma sheet.

However, the fact that the  $H^+$  density in the near-Earth plasma sheet increases with solar EUV flux suggests that low-energy outflow significantly contribute to feed the near-Earth with  $H^+$  ions as there is no evidence of an increase of energetic  $H^+$  outflows and solar wind  $H^+$  entry with solar EUV flux. Furthermore, a significant entry of cold  $O^+$  ions from the high-latitude ionosphere—which flux is very sensitive to solar EUV flux—in the near-Earth region is consistent with the strong modulation of the  $O^+$  density by solar EUV flux at low geocentric distances evidenced in this study.

So we suggest that both cold ion outflow from the high-latitude ionosphere and more energetic outflows from the auroral zone should be considered as potentially significant sources leading to the direct entry of ionospheric ions in the near-Earth plasma sheet. The question of low-energy ions energization as they enter the plasma sheet at low geocentric distances must, however, be taken into account as we consider energies about 1 keV. Indeed, close to Earth, the magnetic field line curvature is relatively low which may limit ionospheric ions energization and question about their capability to reach energies in the keV range.

At higher geocentric distances, we showed that the impact of solar EUV flux on the plasma sheet  $O^+$  density is weaker than at low geocentric distance while the effect of geomagnetic activity is stronger. The  $O^+$  density variation with geomagnetic and solar activity from our study are similar to the variations of the flux of energetic outflowing  $O^+$  ions as reported by *Yau et al.* [1988]. This may signal an increased contribution of energetic  $O^+$  ions at higher geocentric distances, as expected from the velocity filter effect. In the midtail region we do not find a significant correlation between the  $H^+$  density and geomagnetic and solar activity contrary to what has been observed for the flux of  $H^+$  escaping the ionosphere. This suggests that at distances higher than  $15 R_E$ , the ionospheric contribution to the plasma sheet  $H^+$  density may be significantly weaker than the contribution of solar wind  $H^+$ .

## 6.2. Summary

Identifying the source of  $O^+$  ions and assessing the relative contribution of transport and outflow flux on the  $O^+$  content is a complex issue. The statistical density maps provided in this study show the final result of the numerous and interconnected processes associated with the escape, acceleration, and transport of ionospheric ions in the magnetosphere. The mapping technique used in this study provides an efficient way to take advantage of the extended plasma composition measurement from the Cluster spacecraft in order to get a comprehensive outlook of the plasma sheet  $O^+$  and  $H^+$  content and of the ionospheric contribution to the plasma sheet population. The following summarizes our observations:

1. The plasma sheet  $O^+$  density significantly increases when the geomagnetic activity and solar EUV flux increase whatever is the geocentric distance. In contrast, no significant variations of the  $H^+$  density with geomagnetic and solar EUV flux are observed in the midtail and far tail while at low geocentric distance the  $H^+$  density slightly increases with increasing solar EUV flux and geomagnetic activity.
2. The  $O^+$ ,  $H^+$  density and  $O^+/H^+$  density ratios are highly variable everywhere in the magnetosphere, the typical standard deviation of the density being of the same order of magnitude as the density median value. The  $O^+/H^+$  density is particularly variable in the dawnside magnetospheric flank during quiet periods.
3. In the midtail region (distances between  $\sim 15$  and  $20 R_E$ ) the  $O^+$  density depends strongly on geomagnetic activity and less on solar EUV flux. From low to high solar EUV flux levels the  $O^+$  density increases on average by a factor of  $\sim 3.5$ . The effect of geomagnetic activity is strong and modulated by the solar EUV flux level. When  $Kp$  increases from 0 to 7, the  $O^+$  density increases on average by a factor of  $\sim 10$  for low ( $F_{10.7} \leq 100$ ), of  $\sim 19$  for medium ( $100 < F_{10.7} \leq 150$ ), and of  $\sim 31$  for high ( $F_{10.7} > 150$ ) solar EUV flux levels.
4. In the near-Earth regions (distances lower than  $\sim 10 R_E$ ), the effect of geomagnetic activity and solar EUV flux on the  $O^+$  density is comparable. From low ( $Kp = 0$ ) to high ( $Kp = 7$ ) geomagnetic activity levels the average  $O^+$  density increases by about 1 order of magnitude irrespective of the solar EUV flux level. The effect of solar EUV flux on the  $O^+$  density is higher than in the midtail regions and seems to be more pronounced during quiet periods. During periods of low geomagnetic activity ( $Kp \leq 2$ ) the  $O^+$  density increases by a factor of  $\sim 7$  from low to high solar EUV flux while this increase is of a factor of  $\sim 5$  if all geomagnetic activity levels are taken into account.
5. We found no clear indication of a cross tail (i.e., dawn-dusk) dependence of the  $O^+$  and  $H^+$  density and  $O^+/H^+$  density ratio in the midtail region. At low geocentric distances ( $7\text{--}8 R_E$ ), the  $H^+$  and  $O^+$  densities peak in the nightside during periods of quiet and moderate geomagnetic activity. For active periods, this peak is shifted in the morning side. In both cases, there is no significant change of the density ratio as a function of MLT.
6. In the tail, at distances below  $10 R_E$ , the decrease of the  $O^+$  density with geocentric distances is steeper than the decrease of the  $H^+$  density. At higher geocentric distances (between  $10$  and  $20 R_E$ ) they decrease at approximately the same rate, and the  $O^+/H^+$  density ratio is almost constant.

7. There is a significant direct entry of  $O^+$  ions in the near-Earth plasma sheet (below  $\sim 10 R_E$ ). The strong dependence of the  $O^+$  density on solar EUV flux and the increase of  $H^+$  density with solar EUV flux in the near-Earth plasma sheet suggest that both auroral outflow and low-energy outflow from the high-latitude ionosphere may contribute to the direct entry of ionospheric ions in the near-Earth plasma sheet.

### Acknowledgments

The authors are grateful to the engineers and scientist from UNH, MPE, IRAP (ex CESR), MPS, IRF, UCB, and UW who made the development of the CIS experiment possible and to E. Penou for the development of CL, the Cluster CIS software. The  $Kp$  and  $F_{10.7}$  indexes were obtained from the SPIDR database at <http://spidr.ngdc.noaa.gov/spidr/home.do>. Solar wind/IMF data were obtained from the GSFC/SPDF OMNIweb interface at <http://omniweb.gsfc.nasa.gov>. The authors acknowledge ISSI for its support to the International Team « Heavy Ions: Their Dynamical Impact on the Magnetosphere ». R. Maggiolo is supported by a PRODEX/CLUSTER contract (PEA 90096). Work at UNH was supported by NASA under grants NNX11AI39G and NNX11AB65G. R. Maggiolo is grateful to J. De Keyser for helpful discussions.

Masaki Fujimoto thanks the reviewers for their assistance in evaluating this paper.

### References

- Abe, T., B. A. Whalen, A. W. Yau, R. E. Horita, S. Watanabe, and E. Sagawa (1993), EXOS D (Akebono) suprathermal mass spectrometer observations of the polar wind, *J. Geophys. Res.*, *98*(A7), 11,191–11,203, doi:10.1029/92JA01971.
- Abe, T., A. W. Yau, S. Watanabe, M. Yamada, and E. Sagawa (2004), Long-term variation of the polar wind velocity and its implication for the ion acceleration process: Akebono/suprathermal ion mass spectrometer observations, *J. Geophys. Res.*, *109*, A09305, doi:10.1029/2003JA010223.
- Axford, W. I. (1968), The polar wind and the terrestrial helium budget, *J. Geophys. Res.*, *73*, 6855–6859, doi:10.1029/JA073i021p06855.
- Balan, N., G. J. Bailey, and R. J. Moffett (1994), Modeling studies of ionospheric variations during an intense solar cycle, *J. Geophys. Res.*, *99*, 17,467–17,475, doi:10.1029/94JA01262.
- Bouhram, M., B. Klecker, G. Paschmann, S. Haaland, H. Hasegawa, A. Blagau, H. Rème, J.-A. Sauvaud, L. M. Kistler, and A. Balogh (2005), Survey of energetic  $O^+$  ions near the dayside mid-latitude magnetopause with Cluster, *Ann. Geophys.*, *23*, 1281–1294, doi:10.5194/angeo-23-1281-2005.
- Chandler, M. O. (1995), Observations of downward moving  $O^+$  in the polar topside ionosphere, *J. Geophys. Res.*, *100*(A4), 5795–5800, doi:10.1029/94JA03236.
- Chappell, C. R., T. E. Moore, and J. H. Waite Jr. (1987), The ionosphere as a fully adequate source of plasma for the Earth's magnetosphere, *J. Geophys. Res.*, *92*, 5896–5910, doi:10.1029/JA092iA06p05896.
- Chappell, C. R., B. L. Giles, T. E. Moore, D. C. Delcourt, P. D. Craven, and M. O. Chandler (2000), The adequacy of the ionospheric source in supplying magnetospheric plasma, *J. Atmos. Sol. Terr. Phys.*, *62*, 421–436, doi:10.1016/S1364-6826(00)00021-3.
- Cladis, J. B. (1986), Parallel acceleration and transport of ions from polar ionosphere to plasma sheet, *Geophys. Res. Lett.*, *13*, 893–896, doi:10.1029/GL013i009p00893.
- Cully, C. M., E. F. Donovan, Å. W. Yau, and G. G. Arkos (2003a), Akebono/Supratherma Mass Spectrometer observations of low-energy ion outflow: Dependence on magnetic activity and solar wind conditions, *J. Geophys. Res.*, *108*, 1093–1103, doi:10.1029/2002JA009587.
- Cully, C. M., E. F. Donovan, A. W. Yau, and H. J. Oppenorth (2003b), Supply of thermal ionospheric ions to the central plasma sheet, *J. Geophys. Res.*, *108*(A2), 1092, doi:10.1029/2002JA009457.
- Darrrouzet, F., J. De Keyser, P. M. E. Décréau, F. El Lemdani-Mazouz, and X. Vallières (2008), Statistical analysis of plasmaspheric plumes with Cluster/WHISPER observation, *Ann. Geophys.*, *26*, 2403–2417, doi:10.5194/angeo-26-2403-2008.
- Delcourt, D., J.-A. Sauvaud, and A. Pedersen (1990), Dynamics of single particle orbits during substorm expansion phase, *J. Geophys. Res.*, *95*, 20,853–20,865, doi:10.1029/JA095iA12p20853.
- Ebihara, Y., M. Yamada, S. Watanabe, and M. Ejiri (2006), Fate of outflowing suprathermal oxygen ions that originate in the polar ionosphere, *J. Geophys. Res.*, *111*, A04219, doi:10.1029/2005JA011403.
- Elliott, H. A., R. H. Comfort, P. D. Craven, M. O. Chandler, and T. E. Moore (2001), Solar wind influence on the oxygen content of ion outflow in the high-altitude polar cap during solar minimum conditions, *J. Geophys. Res.*, *106*(A4), 6067–6084, doi:10.1029/2000JA003022.
- Engwall, E., A. I. Eriksson, C. M. Cully, M. André, P. A. Puhl-Quinn, H. Vaith, and R. Torbert (2009), Survey of cold ionospheric outflows in the magnetotail, *Ann. Geophys.*, *27*, 3185–3201, doi:10.5194/angeo-27-3185-2009.
- Feynman, J. (1982), Geomagnetic and solar wind cycles, 1900–1975, *J. Geophys. Res.*, *87*, 6153–6162, doi:10.1029/JA087iA08p06153.
- Fujimoto, M., T. Terasawa, T. Mukai, Y. Saito, T. Yamamoto, and S. Kokubun (1998), Plasma entry from the flanks of the near-Earth magnetotail: Geotail observations, *J. Geophys. Res.*, *103*, 4391–4408, doi:10.1029/97JA03340.
- Goertz, C. K., and W. Baumjohann (1991), On the thermodynamics of the plasma sheet, *J. Geophys. Res.*, *96*, 20,991–20,998, doi:10.1029/91JA02128.
- Gurgiolo, C., and J. L. Burch (1982), DE-1 observations of the polar wind—A heated and an unheated component, *Geophys. Res. Lett.*, *9*, 945–948, doi:10.1029/GL009i009p00945.
- Haaland, S., B. Lybekk, K. Svenes, A. Pedersen, M. Förster, H. Vaith, and R. Torbert (2009), Plasma transport in the magnetotail lobes, *Ann. Geophys.*, *27*, 3577–3590, doi:10.5194/angeo-27-3577-2009.
- Haaland, S., et al. (2012), Estimating the capture and loss of cold plasma from ionospheric outflow, *J. Geophys. Res.*, *117*, A07311, doi:10.1029/2012JA017679.
- Hansen, R. T., S. F. Hansen, and C. Sawyer (1976), Long-lived coronal structures and recurrent geomagnetic patterns in 1974, *Planet. Space Sci.*, *24*, 381–388, doi:10.1016/0032-0633(76)90051-9.
- Heelis, R. A., W. R. Coley, M. Loranc, and M. R. Hairston (1992), Three-dimensional ionospheric plasma circulation, *J. Geophys. Res.*, *97*, 13,903–13,910, doi:10.1029/92JA00872.
- Kistler, L. M., E. Mobius, W. Baumjohann, G. Paschmann, and D. C. Hamilton (1992), Pressure changes in the plasma sheet during substorm injections, *J. Geophys. Res.*, *97*, 2973–2983, doi:10.1029/91JA02802.
- Kistler, L. M., C. G. Mouikis, B. Klecker, and I. Dandouras (2010), Cusp as a source for oxygen in the plasma sheet during geomagnetic storms, *J. Geophys. Res.*, *115*, A03209, doi:10.1029/2009JA014838.
- Kitamura, N., et al. (2010), Observations of very-low-energy (<10 eV) ion outflows dominated by  $O^+$  ions in the region of enhanced electron density in the polar cap magnetosphere during geomagnetic storms, *J. Geophys. Res.*, *115*, A00J06, doi:10.1029/2010JA015601.
- Kronberg, E. A., S. E. Haaland, P. W. Daly, E. E. Grigorenko, L. M. Kistler, M. Franz, and I. Dandouras (2012), Oxygen and proton abundance in the near-Earth magnetosphere: Statistical results on the response to the geomagnetic and solar wind activity conditions, *J. Geophys. Res.*, *117*, A12208, doi:10.1029/2012JA018071.
- Lennartsson, W., and E. G. Shelley (1986), Survey of 0.1- to 16-keV/e plasma sheet ion composition, *J. Geophys. Res.*, *91*, 3061–3076, doi:10.1029/JA091iA03p03061.
- Lennartsson, W. (1989), Energetic (0.1- to 16-keV/e) magnetospheric ion composition at different levels of solar F10.7, *J. Geophys. Res.*, *94*(A4), 3600–3610, doi:10.1029/JA094iA04p03600.
- Lennartsson, O. W., H. L. Collin, and W. K. Peterson (2004), Solar wind control of Earth's  $H^+$  and  $O^+$  outflow rates in the 15-eV to 33-keV energy range, *J. Geophys. Res.*, *109*, A12212, doi:10.1029/2004JA010690.

- Liao, J., L. M. Kistler, C. G. Mouikis, B. Klecker, I. Dandouras, and J.-C. Zhang (2010), Statistical study of O<sup>+</sup> transport from the cusp to the lobes with Cluster CODIF data, *J. Geophys. Res.*, *115*, A00J15, doi:10.1029/2010JA015613.
- Liao, J., L. M. Kistler, C. G. Mouikis, B. Klecker, and I. Dandouras (2012), Solar cycle dependence of the cusp O<sup>+</sup> access to the near-Earth magnetotail, *J. Geophys. Res.*, *117*, A10220, doi:10.1029/2012JA017819.
- Lockwood, M., M. O. Chandler, J. L. Horwitz, J. H. Waite Jr., T. E. Moore, and C. R. Chappell (1985), The cleft ion fountain, *J. Geophys. Res.*, *90*, 9736–9748, doi:10.1029/JA090iA10p09736.
- Lotko, W. (2007), The magnetosphere-ionosphere system from the perspective of plasma circulation: A tutorial, *J. Atmos. Sol. Terr. Phys.*, *69*(3), 191–211, doi:10.1016/j.jastp.2006.08.011.
- Lu, G., P. H. Reiff, T. E. Moore, and R. A. Heelis (1992), Upflowing ionospheric ions in the auroral region, *J. Geophys. Res.*, *97*, 16,855–16,863, doi:10.1029/92JA01435.
- Lyons, L. R., and T. W. Speiser (1982), Evidence for current sheet acceleration in the geomagnetic tail, *J. Geophys. Res.*, *87*, 2276–2286, doi:10.1029/JA087iA04p02276.
- Moore, T. E., and D. C. Delcourt (1995), The geopause, *Rev. Geophys.*, *33*(2), 175–209, doi:10.1029/95RG00872.
- Mouikis, C. G., L. M. Kistler, Y. H. Liu, B. Klecker, A. Korth, and I. Dandouras (2010), H<sup>+</sup> and O<sup>+</sup> content of the plasma sheet at 15–19 Re as a function of geomagnetic and solar activity, *J. Geophys. Res.*, *115*, A00J16, doi:10.1029/2010JA015978.
- Newell, P. T., C.-I. Meng, and K. M. Lyons (1996), Suppression of discrete aurora by sunlight, *Nature*, *381*, 766–767, doi:10.1038/381766a0.
- Newell, P. T., C.-I. Meng, and S. Wing (1998), Relation to solar activity of intense aurorae in sunlight and darkness, *Nature*, *393*, 342–344, doi:10.1038/30682/.
- Newell, P. T., and S. Wing (2000), Remotely imaging the plasma sheet with low-altitude satellite clusters, *J. Atmos. Sol. Terr. Phys.*, *62*, 851–863, doi:10.1029/2009JA014326.
- Newell, P. T., T. Sotirelis, and S. Wing (2009), Diffuse, monoenergetic, and broadband aurora: The global precipitation budget, *J. Geophys. Res.*, *114*, A09207, doi:10.1029/2009JA014326.
- Nilsson, H., E. Engwall, A. Eriksson, P. A. Puhl-Quinn, and S. Arvelius (2010), Centrifugal acceleration in the magnetotail lobes, *Ann. Geophys.*, *28*, 569–576, doi:10.5194/angeo-28-569-2010.
- Nilsson, H., I. A. Barghouthi, R. Slapak, A. I. Eriksson, and M. André (2012), Hot and cold ion outflow: Spatial distribution of ion heating, *J. Geophys. Res.*, *117*, A11201, doi:10.1029/2012JA017974.
- Nishino, M. N., M. Fujimoto, T.-D. Phan, T. Mukai, Y. Saito, M. M. Kuznetsova, and L. Rastätter (2005), Anomalous flow deflection at Earth's low-Alfvén-Mach-number bow shock, *Phys. Rev. Lett.*, *101*, doi:10.1103/PhysRevLett.101.065003.
- Norqvist, P., M. André, and M. Tyrlund (1998), A statistical study of ion energization mechanisms in the auroral region, *J. Geophys. Res.*, *103*, 23,459–23,473, doi:10.1029/98JA02076.
- Nosé, M., A. Ieda, and S. P. Christon (2009), Geotail observations of plasma sheet ion composition over 16 years: On variations of average plasma ion mass and O<sup>+</sup> triggering substorm model, *J. Geophys. Res.*, *114*, A07223, doi:10.1029/2009JA014203.
- Ohtani, S., M. Nosé, S. P. Christon, and A. T. Y. Lui (2011), Energetic O<sup>+</sup> and H<sup>+</sup> ions in the plasma sheet: Implications for the transport of ionospheric ions, *J. Geophys. Res.*, *116*, A10211, doi:10.1029/2011JA016532.
- Peterson, W. K., H. L. Collin, O. W. Lennartsson, and A. W. Yau (2006), Quiet time solar illumination effects on the fluxes and characteristic energies of ionospheric outflow, *J. Geophys. Res.*, *111*, A11505, doi:10.1029/2005JA011596.
- Peterson, W. K., L. Andersson, B. C. Callahan, H. L. Collin, J. D. Scudder, and A. W. Yau (2008), Solar-minimum quiet time ion energization and outflow in dynamic boundary related coordinates, *J. Geophys. Res.*, *A07222*, doi:10.1029/2008JA013059.
- Pulkkinen, T. I., and N. A. Tsyganenko (1996), Testing the accuracy of magnetospheric model field line mapping, *J. Geophys. Res.*, *101*(A12), 27,431–27,442, doi:10.1029/96JA02489.
- Rème, H., et al. (2001), First multispacecraft ion measurements in and near the Earth's magnetosphere with the identical Cluster Ion Spectrometry (CIS) experiment, *Ann. Geophys.*, *19*, 1303–1354, doi:10.5194/angeo-19-1303-2001.
- Sergeev, V. A., M. Malkov, and K. Mursula (1993), Testing the isotropic boundary algorithm method to evaluate the magnetic field configuration in the tail, *J. Geophys. Res.*, *98*, 7609–7620, doi:10.1029/92JA02587.
- Sergeev, V. A., and B. B. Gvozdevsky (1995), Mt-index—A possible new index to characterize the magnetic configuration of the magnetotail, *Ann. Geophys.*, *13*, 1093–1103, doi:10.1007/s00585-995-1093-9.
- Shelley, E. G., R. G. Johnson, and R. D. Sharp (1972), Satellite observations of energetic heavy ions during a geomagnetic storm, *J. Geophys. Res.*, *77*, 6104–6110, doi:10.1029/JA077i031p06104.
- Shevchenko, I. G., V. Sergeev, M. Kubyshkina, V. Angelopoulos, K. H. Glassmeier, and H. J. Singer (2010), Estimation of magnetosphere-ionosphere mapping accuracy using isotropy boundary and THEMIS observations, *J. Geophys. Res.*, *115*, A11206, doi:10.1029/2010JA015354.
- Spence, H. E., M. G. Kivelson, R. J. Walker, and D. J. McComas (1989), Magnetotail plasma pressures in the midnight meridian: Observations, *J. Geophys. Res.*, *94*(A5), 5264–5272, doi:10.1029/JA094iA05p05264.
- Su, Y.-J., J. L. Horwitz, T. E. Moore, B. L. Giles, M. O. Chandler, P. D. Craven, M. Hiraehara, and C. J. Pollock (1998), Polar wind survey with the Thermal Ion Dynamics Experiment/Plasma Source Instrument suite aboard POLAR, *J. Geophys. Res.*, *103*(A12), 29,305–29,337, doi:10.1029/98JA02662.
- Terasawa, T., et al. (1997), Solar wind control of density and temperature in the near-Earth plasma sheet: WIND/GEOTAIL collaboration, *Geophys. Res. Letters*, *24*, 935–938, doi:10.1029/96GL04018.
- Tsyganenko, N. A. (1995), Modeling the Earth's magnetospheric magnetic field confined within a realistic magnetopause, *J. Geophys. Res.*, *100*, 5599–5612, doi:10.1029/94JA03193.
- Tsyganenko, N. A., and D. P. Stern (1996), Modeling the global magnetic field of the large-scale Birkeland current systems, *J. Geophys. Res.*, *101*, 27,187–27,198, doi:10.1029/96JA02735.
- Wahlund, J.-E., H. J. Opgenoorth, I. Häggström, K. J. Winser, and G. O. L. Jones (1992), EISCAT observations of topside ionospheric ion outflows during auroral activity: Revisited, *J. Geophys. Res.*, *97*, 3019–3037, doi:10.1029/91JA02438.
- Wing, S., and P. T. Newell (1998), Central plasma sheet ion properties as inferred from ionospheric observations, *J. Geophys. Res.*, *103*, 6785–6800, doi:10.1029/97JA02994.
- Wing, S., and P. T. Newell (2002), 2D plasma sheet ion density and temperature profiles for northward and southward IMF, *Geophys. Res. Lett.*, *29*(9), 1307, doi:10.1029/2001GL013950.
- Wing, S., J. R. Johnson, P. T. Newell, and C.-I. Meng (2005), Dawn-dusk asymmetry in the northward IMF plasma sheet, *J. Geophys. Res.*, *110*, A08205, doi:10.1029/2005JA011086.
- Yau, A. W., P. Beckwith, W. K. Peterson, and E. G. Shelley (1985a), Long-term (solar cycle) and seasonal variations of upflowing ionospheric ion events at DE-1 altitudes: Magnitude, composition, magnetic activity dependence and long-term variations, *J. Geophys. Res.*, *90*, 6395–6407, doi:10.1029/JA090iA07p06395.

- Yau, A. W., E. G. Shelley, W. K. Peterson, and L. Lenchyshyn (1985b), Energetic auroral and polar ion outflow at DE-1 altitudes: Magnitude, composition, magnetic activity dependence and long-term variations, *J. Geophys. Res.*, *90*, 8417–8432, doi:10.1029/JA090iA09p08417.
- Yau, A. W., W. K. Peterson, and E. G. Shelley (1988), Quantitative parametrization of energetic ionospheric ion outflow: Modeling magnetospheric plasma, *Geophys. Monogr. Ser.*, *44*, 211–217, doi:10.1029/GM044p0211.
- Yau, A. W., and M. Andre (1997), Sources of ion outflow in the high latitude ionosphere, *Space Sci. Rev.*, *80*, 1–25, doi:10.1023/A:1004947203046.
- Yau, A. W., T. Abe, and W. K. Peterson (2007), The polar wind: Recent observation, *J. Atmos. Sol. Terr. Phys.*, *69*, 1936–1983, doi:10.1016/j.jastp.2007.08.010.
- Yau, A. W., A. Howarth, W. K. Peterson, and T. Abe (2012), Transport of thermal-energy ionospheric oxygen (O<sup>+</sup>) ions between the ionosphere and the plasma sheet and ring current at quiet times preceding magnetic storms, *J. Geophys. Res.*, *117*, A07215, doi:10.1029/2012JA017803.
- Young, D. T., H. Balsiger, and J. Geiss (1982), Correlations of magnetospheric ion composition with geomagnetic and solar activity, *J. Geophys. Res.*, *87*(A11), 9077–9096, doi:10.1029/JA087iA11p09077.